A Strain Energy Density Design Approach for Large Cast Iron Components: From Microstructural Analysis to Multiaxial Fatigue Response

M. Pedranz[1*], V. Fontanari[1], C. Santus[2], D. Lusuardi[3], F. Berto[4], M. Benedetti[1]

[1]*Department of Industrial Engineering, University of Trento, Trento, Italy*

[2]*Department of Civil and Industrial Engineering, University of Pisa, Pisa, Italy*

[3]*Fonderie Ariotti, Adro (BS), Italy*

[4]*Department of Chemical Engineering Materials Environment, Sapienza University, Roma, Italy*

*Corresponding author

Matteo Pedranz

matteo.pedranz@unitn.it

Abstract

A new criterion for predicting multiaxial fatigue in plain and V-notched specimens made of ductile cast iron is proposed. The criterion is based on volumetric strain energy density (SED) and separately accounts for the effect of normal and shear mean stresses with two material-dependent coefficients. The criterion also considers the impact of out-of-phase loading through a strengthening factor, assuming that fatigue damage is initiated by the total SED peak in the cycle. The criterion is validated using a large amount of independent multiaxial fatigue data, obtained from testing three different ductile cast iron grades.

Keywords

Ductile Cast Iron, Multiaxial Fatigue, Strain Energy Density, Mean Stress Effect, Nonproportional Loading

Nomenclature

$2\bar{\alpha}$	notch opening angle
α, β	material-dependent parameters accounting for the mode I and III mean stress effect
ε_{tot}	strain at failure
θ	angle defining the evolution of the loading cycle

λ	multiaxiality ratio
λ_{th}	threshold λ defining the transition from mode I to III dominated fatigue failure
ν	Poisson's ratio
$\sigma_{1,2}$	principal stresses
σ_a, τ_a	axial and shear stress amplitudes
σ_a^*, τ_a^*	mode I and III intrinsic fatigue strengths
$\sigma_{a,N}, \tau_{a,N}$	mode I and III notch fatigue strengths
$\sigma_{a,plain}, \tau_{a,plain}$	mode I and III plain fatigue strengths
$\sigma_{min}, \sigma_{max}$	minimum and maximum axial stresses
$\sigma_{y,02}$	yield strength
τ_{min}, τ_{max}	minimum and maximum shear stresses
φ	phase angle between the axial and torsional loadings
Ω_1, Ω_3	mode I and III SED control volumes
$\sqrt{area}$	geometrical parameter of the defect
C_W	correction coefficient accounting for the mean stress effect
D	notched specimen bar diameter
DCI	ductile cast iron
$d_{F,nodule}$	mean of the graphite nodules maximum Feret diameters
$d_{F,pore}$	shrinkage pore maximum Feret diameter
E	elastic modulus (Young's modulus)
f	modulating function defining the transition from mode I to III dominated fatigue failure
$f_{1,inversion}, f_{3,inversion}$	mode I and III inversion functions for the determination of R_1 and R_3
G	shear modulus
HB	Brinell hardness
HSi	high Si content DCI ferritic grade
$K_{f,N1}, K_{f,N3}$	mode I and III notch fatigue stress concentration factors
k_φ	phase correction factor accounting for the phase effect

2

N_f	number of cycles to failure
R_N	notch radius
R	stress (or load) ratio
R_1, R_3	mode I and III SED control radii
RMS	root mean square
S	standard deviation
SED	strain energy density
SED_{peak}	peak strain energy density values in the cycle
$\Delta\,SED_{peak}$	difference between the peaks strain energy density values
UTS	ultimate tensile strength
$\overline{W}_{1,plain}, \overline{W}_{3,plain}$	mode I and III SED associated to the plain fatigue strengths
$\overline{W}_1^*, \overline{W}_3^*$	mode I and III SED associated to the intrinsic fatigue strengths
$\overline{W}_{1,eq}, \overline{W}_{3,eq}$	mode I and III equivalent SED
$\overline{W}_{1,U}, \overline{W}_{3,U}$	mode I and III SED for unitary applied nominal stress

1. Introduction

The expanding energy industry has spurred a growing demand for ductile cast iron (DCI), also known as nodular cast iron, due to its unique material properties such as low melting point and good fluidity, which enable good castability for complex and large components [1]. Examples include windmill parts, nuclear waste storage containers, cement production components, and bench presses. However, large components' low cooling rates often result in casting defects like degenerated graphite and micro-porosity [2]. To address this, spheroidization treatment with magnesium and the addition of rare earths to the cast can reduce graphite degeneration [3,4]. The size and distribution of shrinkage pores depend on DCI grade and cooling rate, but their formation can be mitigated by placing chillers in critical zones, namely those affected by the lowest cooling rates. Moreover, components are typically subjected to multiaxial and time-varying loading, thus requiring the adoption of suitable multiaxial fatigue criteria for safe design.

Early approaches to design against multiaxial fatigue were empirical, relying on fitting experimental data [5]. However, these approaches were limited in applicability to the stress states and the geometries that were actually tested [5]. As a result, researchers turned to theoretical approaches that could be generally applied to any geometry and loading condition. Stress invariants-based criteria [6,7] are based on exploiting the hydrostatic stress and the second invariant of the deviatoric stress tensor. However, they can only be applied to proportional loadings and, therefore, have been largely replaced by other multiaxial fatigue calculation methods. Critical plane-based approaches [8–22] involve strain-based, stress-based, or strain/stress-based criteria and rely on a "critical" plane, where a certain stress component, strain component, or a combination of both displays its maximum value. Energetic approaches involve

transforming specific stress and strain components, or energies, into equivalent damage parameters associated with a uniaxial fatigue curve [20,23–29].

In this paper, we will specifically focus on strain energy density (SED)-based approaches, which offer several advantages over other multiaxial fatigue calculation methods. Firstly, the effect of stress gradients is implicitly considered in the volumetric SED [30]. Secondly, the problem of defining a critical plane is completely bypassed. The SED is indeed a scalar quantity that is averaged over a control volume whose size is material-dependent (recalling the "elementary volume" and "structural support length" of Neuber [30,31]). Working with scalars reduces the computational power required for the fatigue assessments and simplify the method on a conceptual point of view, making its application more suitable for industries. The base idea, proposed by Lazzarin and Zambardi [32], states that fatigue failure in a notched component happens when the SED, evaluated over a control volume, reaches a critical value, which is a characteristic feature of the material and of the loading mode. For plane or axisymmetric problems, the control volume simplifies into a circular domain, as schematically illustrated in Fig. 1.
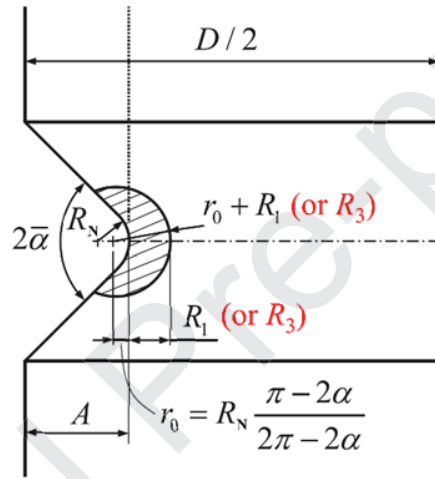

Figure 1. Schematic representation of the mode I or mode III SED critical volumes.

The circular sector encompassing the notch tip is centered in the origin of the curvilinear reference frame used to describe the notch geometry and located at distance r_0 from the notch tip moving along the notch bisector. The radius r_0 is a function of notch radius R_N and opening angle $2\bar{\alpha}$. To account for different notch sensitivity displayed by several materials to type I and III mode of loading, Berto et al. [30] proposed to average mode I and III SED components, over control volume characterized by a distinct value of radius, denoted in Fig. 1 as R_1 and R_3, respectively. The mode III type of loading is typically associated with lower notch sensitivity, which can be attributed to the peculiar "factory roof" fracture morphology found in notched specimens loaded under torsion. This phenomenon has been extensively studied by Berto et al. [33] and Tanaka et al. [34], who associated the factory roof fracture with rubbing and abrasion, resulting in energy dissipation. They proposed the concept of mode III notch-strengthening effect produced by cyclic crack surface contact, which explains the abrasion and debris formation.

In the classical formulation of the method, the fatigue damage is linked to the variation between maximum and minimum SED occurring during the load cycle. The mean stress effect is considered by means of a correction coefficient c_w [35] that is equal to 1 and 0.5 for the stress ratio R=0 and R=-1, respectively. As a result, the fatigue strength range for the nominal ratio R=-1, increases according to a factor $\sqrt{2}$ with respect

4

to case corresponding to R=0, in agreement with the recommendations provided by the Eurocode 3 and IIW for stress- relieved welded joints. The SED fatigue criterion devised so far can be formulated in this way:

$$\begin{cases} c_w \cdot \overline{W}_{1,\text{notch}}(R_1) + c_w \cdot \overline{W}_{3,\text{notch}}(R_3) = \overline{W}_{1,\text{plain}} \\ c_w = \begin{cases} \frac{1+R^2}{(1-R)^2} & \text{for} \quad -\infty \le R < 0 \\ 1 & \text{for} \quad R = 0 \\ \frac{1-R^2}{(1-R)^2} & \text{for} \quad 0 < R < 1 \end{cases} \end{cases} \tag{1}$$

where c_w is the correction coefficient for the mean stress effect (considered to be the same for mode I and III loading), R is the stress ratio, $\overline{W}_{1,\text{plain}}$ is the SED of plain specimens under mode I loading, and, finally, $\overline{W}_{1,\text{notch}}$ and $\overline{W}_{3,\text{notch}}$ are the notch SEDs for mode I and mode III loading, which are function of the SED control radii R_1 and R_3. Atzori et al. [36] and Berto et al. [33] successfully applied the strain energy density (SED) method to compile a comprehensive collection of multiaxial fatigue data from axisymmetric V-notched specimens made of C40 steel, 39NiCrMo3 hardened and tempered steel, and Ti-6Al-4V alloy. However, despite these achievements, the existing SED-based fatigue calculation framework faces some limitations.

Firstly, it does not consider the varying mean stress sensitivity displayed by different structural metals. To address this issue, Benedetti et al. [37] recently proposed an alternative method to incorporate the mean stress effect into an SED-based fatigue criterion. By integrating the range and maximum value of average SED into a Walker-like equation, an equivalent fatigue damage parameter can be expressed. The mean stress sensitivity factor α was found to significantly differ among Al alloys, quenched and tempered steels, and cast irons and to be strongly dependent on the fatigue life regime.

Secondly, the application of the SED approach to multiaxial notch fatigue strength assessment raises the challenge of accounting for the effects of non-proportional loading. The sensitivity to the phase angle is influenced by the material's microstructure and notch acuity. Marangon et al. [38] analyzed multiaxial fatigue data of steel specimens and provided insightful observations. They demonstrated that under a nominal load ratio of R=-1, the most damaging configuration was the 90° out-of-phase loading, which reduced fatigue strength by 6-13% compared to in-phase loading. The phase angle's influence was found to be more pronounced at lower biaxiality ratios, and a similar trend was detected for a load ratio of R=0. Additionally, the phase angle's effect was found to be slightly dependent on the notch opening angle and the material characteristic length.

Furthermore, the reduction in fatigue strength of steel specimens due to out-of-phase loading aligns with the findings of Sonsino et al. [39,40]. The "factory roof" morphology was also observed in notched specimens tested under multiaxial fatigue, with slight variations in morphology depending on the phase angle. Non-proportional out-of-phase loading influences the experimentally measured fatigue strength, but this effect is strongly influenced by the tested material. Benedetti et al. [2], Berto et al. [41], and Tovo et al. [42] observed a strengthening effect due to out-of-phase loading in both plain and notched specimens made of ductile cast iron (DCI), while out-of-phase loading seemingly weakened specimens made of steel. Itoh et al. [43] reported that the decrease in fatigue strength due to non-proportional loading depends on the tested material's crystal structure. However, these aspects have not yet been incorporated into SED-based fatigue approaches.

To conclude, another aspect must be considered when applying a multiaxial fatigue criterion to predict plain and notch fatigue strengths of ductile cast iron (DCI), particularly for heavy-section pearlitic DCI. Indeed, Benedetti et al. [44] observed that in plain specimens, fatigue damage was triggered by shrinkage pores, while in notched specimens, it was initiated by graphite nodules located near the notch tip. A plausible

5

explanation, which will be further substantiated in this work, is that the highly stressed volume (HSV) in plain specimens is sufficiently large to encompass, from a probabilistic perspective, significant shrinkage pores [45]. Conversely, the HSV in notched specimens might be too small to include pores more critical than graphite nodules. This evidence highlights the necessity to define an intrinsic fatigue strength, representing a pore-free material. Essentially, the intrinsic fatigue strength accounts for all homogeneously distributed microstructural features within the material, such as the microstructure (ferritic, pearlitic, ferritic-pearlitic, etc.) and graphite nodules. Shrinkage pores, on the other hand, are unevenly and randomly distributed on a microscopic scale and, therefore, should be addressed using a probabilistic approach.

In this work, we introduce a novel SED-based multiaxial fatigue criterion capable of addressing both the mean stress effect and the phase effect. The implementation of the criterion is carried out in elastic conditions. The criterion's validation is demonstrated using independent sets of experimental data obtained from testing three distinct DCI grades subjected to multiaxial fatigue loading. The paper is structured as follows: Section 2 outlines the investigated materials and highlights their unique microstructure-related fatigue properties, which must be incorporated into the modified SED-based multiaxial fatigue criterion. Section 3 details the experimental procedures employed in conducting the fatigue tests. The proposed multiaxial fatigue criterion is presented in Section 4, while Section 5 is devoted to validating the criterion using independent sets of experimental multiaxial fatigue data. Finally, Section 6 summarizes the most significant conclusions and observations.

2. Materials

The experimental campaign was carried out on three different cast iron grades, namely a EN-GJS-600-3 DCI with pearlitic matrix, a EN-GJS-450-18 DCI with high Si content (regarded as High-Si or HSi) and ferritic matrix. Some of the data related to the EN-GJS-600-3 grade were already presented in [2], while in this work, we present supplementary data obtained from multiaxial fatigue testing, which is crucial for validating the proposed criterion.[41] Conversely, the data related to the HSi grade are reported in this work for the first time. The discussion is enriched by the dataset collected in an independent previous work carried out in [2] on an EN-GJS-400-18-LT DCI with ferritic-pearlitic matrix. The micrographs of the investigated materials, shown in Fig. 2, were obtained by means of an optical microscope, polishing samples extracted close to the fracture surfaces of the tested fatigue specimens. It must be pointed out that the HSi grade was optimized by the foundry for large casts to provide the required mechanical properties and considering the specific requests of customers and designers.
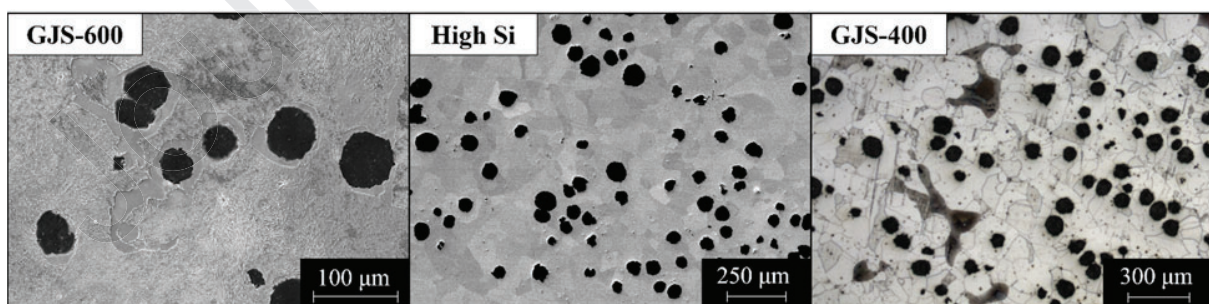

Figure 2. *Micrographs of the three investigated DCI grades, showing the respective microstructures.*

The chemical compositions and the mechanical properties of the three investigated grades are reported in Table 1.

Table 1. Chemical composition and main mechanical properties of the three investigated DCI grades.

	C (%)	Si (%)	Mn (%)	P (%)	S (%)	Cu (%)	Ni (%)	Mg (%)
GJS-600	3.55	2.39	0.28	0.038	0.009	0.52	0.02	0.046
HSi	3.43	3.57	0.19	0.04	0.009	0.06	0.02	0.043
GJS-400 [46]	3.50	2.45	0.12	0.02	0.007	0.13	0.03	0.055

	E (GPa)	G (GPa)	$\sigma_{y,0.2}$ (MPa)	UTS (MPa)	ε_{tot} (%)	Poisson's ratio	HB
GJS-600	174 ± 2	68.5 ± 1.3	363 ± 8	485 ± 15	2.1 ± 0.5	0.27	198 ± 4
HSi	174 ± 2	68.5 ± 1.3	364 ± 4	476 ± 3	14.4 ± 2.8	0.27	170 ± 2
GJS-400 [46]	174 ± 2	68.5 ± 1.3	267	378	11.5	0.27	145

The detailed description of the solidification conditions of the GJ-600 and the High Si grades can be found in [44]. Basically, the fatigue specimens were extracted from as-cast cylinders of high thermal modulus (about 6 cm), with diameter of 300 mm and height of 520 mm, exposed to air convection. The solidification time is long enough to be representative of actual thick-walled components. Further details about the production process of the GJS-400 grade are reported in [41]. To summarize them, casting blocks, provided with feeders on the top, and with dimensions $300 \times 250 \times 300$ mm^3, were produced. The specimens for mechanical tests were extracted from the zone with the longest solidification time, therefore representative of real thick-walled casts.

3. Experimental method and campaign

The fatigue data were collected by testing the axisymmetric specimen geometries shown in Fig. 3(a-k). Specimens (a-i) were produced in the GJS-600 and High-Si grades, while specimens (j-k) were produced in the GJS-400 grade. The plain specimens (Fig. 3a, b and j) were tested to collect the materials' baselines fatigue curves. The V-notched specimens (Fig. 3c-i) were appositely designed to optimize the stress state

and maximize the intensity of the asymptotic stress filed and therefore to reduce the uncertainty in the inverse search of the control radii [47,48].
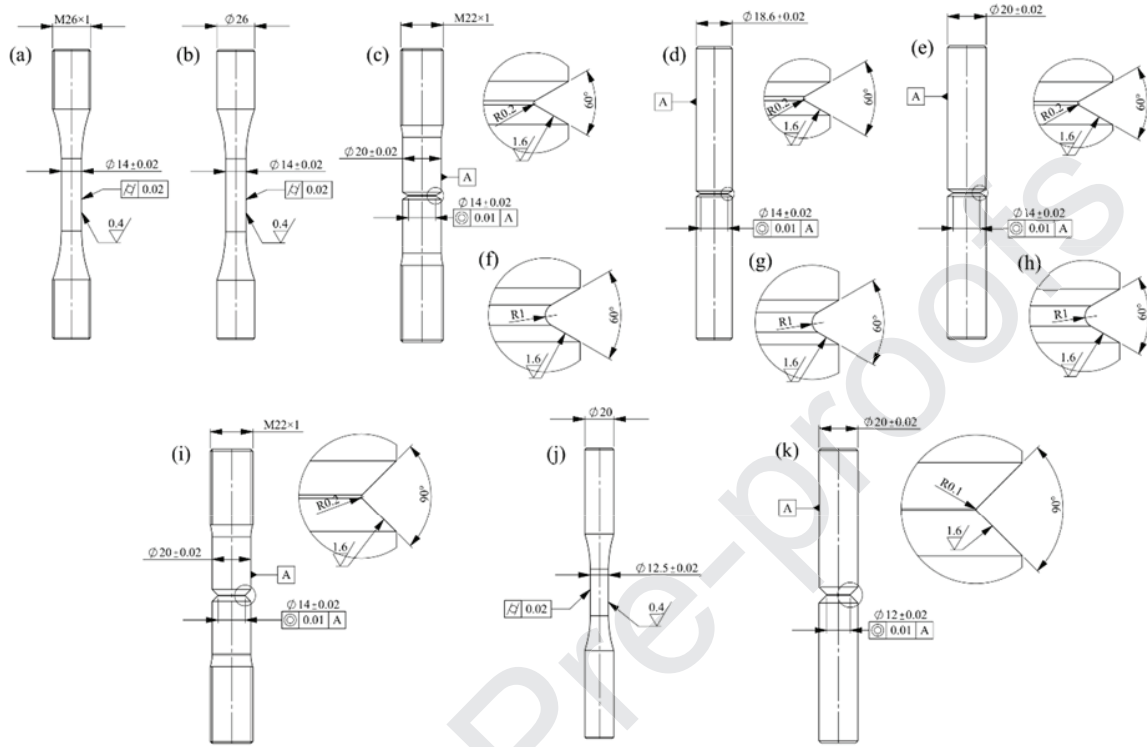

Figure 3. *Technical drawings of the specimens exploited in the fatigue tests: (a) plain specimen for axial tests, (b) plain specimen for torsional and multiaxial tests, (c) V-notched specimen with sharp notch radius and opening angle 2ᾱ of 60° for axial tests, (d) V-notched specimen with sharp notch radius and opening angle 2ᾱ of 60° for torsional tests, (e) V-notched specimen with sharp notch radius and opening angle 2ᾱ of 60° for multiaxial tests, (f) V-notched specimen with blunt notch radius and opening angle 2ᾱ of 60° for axial tests, (g) V-notched specimen with blunt notch radius and opening angle 2ᾱ of 60° for torsional tests, (h) V-notched specimen with blunt notch radius and opening angle 2ᾱ of 60° for multiaxial tests, (i) V-notched specimen with sharp notch radius and opening angle 2ᾱ of 90° for axial tests, (j) plain specimen for axial, torsional and multiaxial tests of the GJS-400 grade, and (k) V-notched specimen with sharp notch radius and opening angle 2ᾱ of 60° for axial, torsional and multiaxial tests of the GJS-400 grade.*

Because of the great influence that the notch radius has on the stress field in notched specimens, the actual notch radii were measured by stereomicroscopy and reported in Table 2.

Table 2. Notch radii measured by stereomicroscopy for the investigated geometries.

Geometry	Nominal notch radius (mm)	Measured notch radius (mm)
Sharp notch (c)	0.2	0.30

Sharp notch (d)	0.2	0.23
Sharp notch (e)	0.2	0.23
Blunt notch (f)	1	1
Blunt notch (g)	1	1
Blunt notch (h)	1	1
Sharp notch (i)	0.2	0.22
Sharp notch (k)	0.1	0.092

The medium-to-high-cycle fatigue life was explored between about 5×10^4 and 5×10^6 cycles to failure and a stress amplitude range between 40 and 300 MPa. The stress amplitudes indicate the nominal stress amplitude in the net cross section. Specimens (a), (c), (f) and (i) were tested under axial loading using two Rumul (Switzerland) Testronic resonant testing machines, at a nominal frequency of 150 Hz, under load control, equipped with load cells of 150 kN and 50 kN load capacity. Specimens (b), (d-e) and (g-h) were tested under torsional and multiaxial loading using a Walter + Bai (Switzerland) LFV100-T1000-HH biaxial servo-hydraulic testing machine equipped with hydraulic grips and a biaxial load cell with axial and torsional load capacities of 100 kN and 1000 Nm, respectively, at a frequency between 15 and 20 Hz. Specimens (j) and (k) were tested under axial, torsional and multiaxial loading, using an MTS 809 servo-hydraulic biaxial machine with a 100 kN axial load cell and a 1100 Nm torsion load, at frequency between 3 and 10 Hz [41]. All data pertaining to axial and torsional loading are displayed in Figure 4 and detailed in Appendix A. A subset of this fatigue data will be employed to calibrate the multiaxial fatigue criterion, as elucidated subsequently. The multiaxial fatigue data, on the other hand, constitutes an independent dataset that is not utilized for criterion calibration but is employed to evaluate the accuracy of fatigue predictions in terms of stress amplitude and the number of cycles to failure. This data will be thoroughly presented in Section 4 and serve as the basis for validating the proposed criterion.
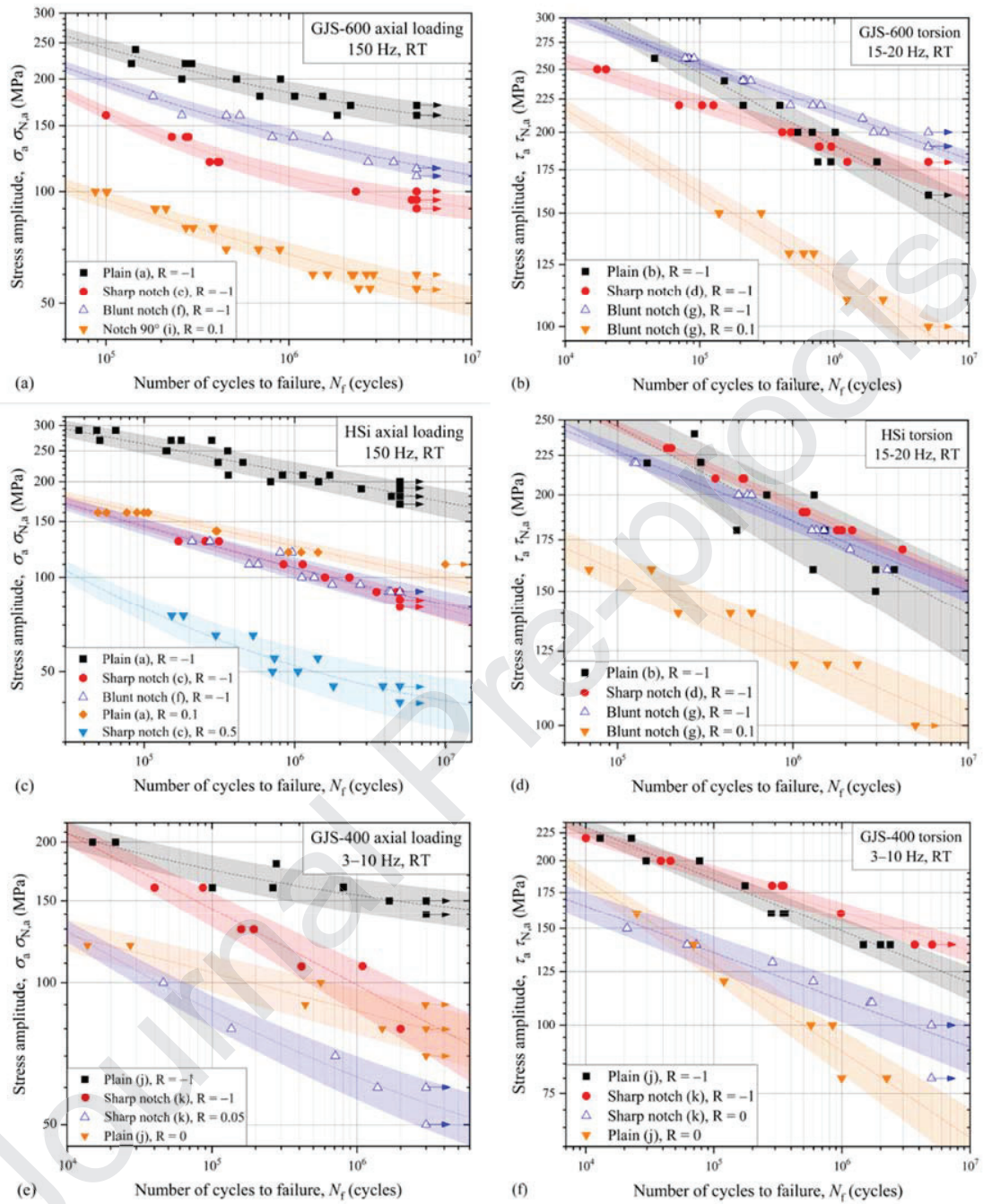
Figure 4. *Axial and torsional fatigue data collected by testing the (a-b) GJS-600 grade, (c-d) HSi grade and (e-f) GJS-400 grade* [41,42]*, at room temperature and with a nominal frequency of 150 Hz or 3-20 Hz, for axial and torsional tests, respectively. The solid lines represent the experimental 50 % failure probability, while the colored bands the 10 to 90 % failure probability.*

The axial fatigue curves indicating the 50 % failure probability are represented by the following asymptotic equation, which can capture the knee observed in the experimental axial fatigue data:

$$\sigma_{\mathrm{a}} = k_1 + \frac{k_2}{N_f^{k_3}} \tag{2}$$

This formulation was introduced by Stromeyer as a modification of the well-known Basquin equation [49]. The addition of an asymptotic term is useful to represent the real behavior of the tested materials, and basically substitute the use of a knee-point, which is the commonly adopted approach [50]. As the torsional and multiaxial fatigue data, as it will be shown later in this work, do not display any knee, the corresponding 50 % failure probability curves is instead well represented by the well-known Basquin's law:

$$\tau_{\mathrm{a}} = \frac{k_2}{N_{\mathrm{f}}^{k_3}}; \qquad \sigma_{\mathrm{a}} = \frac{k_2}{N_{\mathrm{f}}^{k_3}} \tag{3}$$

The scatter of the experimental data was determined by assessing the estimated regression variance, considered to be non-varying in the whole investigated fatigue range, and defined as:

$$S^2 = \frac{\sum_{i=1}^{n}(\sigma_{\mathrm{a,i}} - \hat{\sigma}_{\mathrm{a,i}})^2}{n-p}; \qquad S^2 = \frac{\sum_{i=1}^{n}(\tau_{\mathrm{a,i}} - \hat{\tau}_{\mathrm{a,i}})^2}{n-p} \tag{4}$$

where $\sigma_{a,i}$ and $\tau_{a,i}$ are the i-th fatigue data point, $\hat{\sigma}_{\mathrm{a,i}}$ and $\hat{\tau}_{\mathrm{a,i}}$ are their estimators, n is the number of experimental data points and p is the number of parameters in the regression (2 or 3 in the present case). As previously highlighted in the introduction, it is crucial to consider numerous factors when designing fatigue-resistant components made of ductile cast iron (DCI). Figure 5 presents a comprehensive overview of the key characteristics for the studied DCI grades, as gathered throughout our experimental investigation.
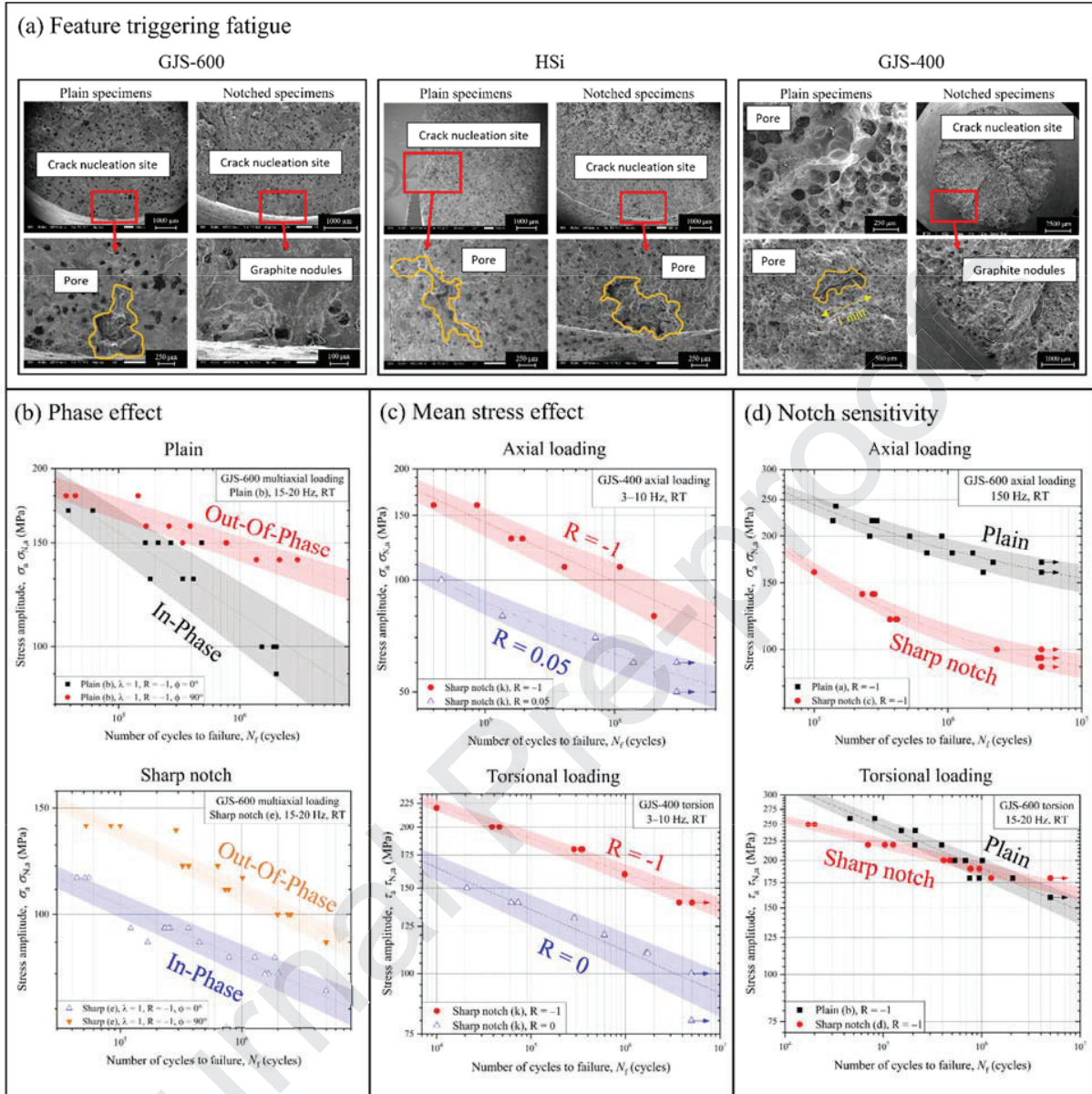
Figure 5. *Schematic representation of peculiar characteristics of the investigated DCI grades. (a) diverse features triggering fatigue failure (micro-shrinkage porosity or graphite nodules); remarkable (b) load phase and (c) the mean stress effect; (d) the different notch sensitivity under mode I and mode III loading.*

Figure 5a displays the fractographic analysis conducted using a JEOL JSM-IT300LV scanning electron microscope (SEM). Previous studies [2,41,51] have provided experimental evidence that fatigue failure can be initiated by shrinkage pores or graphite nodules, depending on the material and specimen geometry. In the case of GJS-600 and GJS-400 grades, fatigue cracks in plain specimens originated from pores, whereas in notched specimens, they began at graphite nodules near the notch tip, as previously demonstrated in [2] and further explained in our recent publication [45].

The probability of encountering a shrinkage pore in a highly stressed volume is influenced by both the component's geometry and the distribution of pores within the material. For notched specimens, the size of the critical defect (with a 99% cumulative probability) in the highly stressed volume is small enough to be inactive compared to the notch, which exhibits a higher fatigue stress concentration factor. However, in plain specimens, the critical defect in the highly stressed volume is large enough to affect fatigue properties, being the highly stressed volume much larger. To design a notched component with suitable fatigue resistance (assuming the notch is severe enough to prevent pore-notch interactions), the reference fatigue strength should correspond to that of pore-free material. An intrinsic fatigue strength [2,45] can be introduced to represent the pore-free material, with the determination framework detailed in [2] and revisited later in this work. In contrast, fatigue failure in the HSi grade consistently originated from shrinkage pores, regardless of the geometry being studied. This outcome is closely tied to the material-dependent distribution of shrinkage pores. In the HSi grade, pores are homogeneously distributed throughout the material at a scale comparable to that of the notches, making them a characteristic feature like graphite nodules. The unique pore distribution in the HSi grade is likely linked to its chemical composition. The high silicon content lowers the eutectic point for carbon, necessitating a reduction in carbon content to achieve the eutectic chemical composition. Graphite nodule expansion during solidification is known to counteract shrinkage pore formation in ductile cast iron [52]. It is logical that lower carbon content leads to reduced graphite content and, consequently, less expansion due to graphite nodule growth. This results in a denser pore distribution within the ductile cast iron. Since the defect initiating fatigue is independent of geometry, the reference fatigue strength for the HSi grade should be based on that of plain specimens.

The effect of the phase angle in the presence of non-proportional loadings is emphasized in Fig. 5b for the GJS-600 grade ductile cast iron (DCI). This trend was also noted in the other investigated DCI grades. It is evident that the phase angle φ significantly affects the fatigue properties of the material. Out-of-phase loading enhances the fatigue strength of both plain and notched specimens, irrespective of the notch geometry. This finding contrasts with the behavior of other metallic materials, such as steels, where out-of-phase loading typically has adverse effects. However, the observed strengthening effect in DCIs is supported by several studies [41,42,53–57]. As a result, it can be hypothesized that in brittle metallic materials, where fatigue damage primarily results from maximum normal stresses, out-of-phase loading is advantageous for fatigue strength [55].

The influence of mean stresses on the GJS-400 grade is illustrated in Fig. 5c, with similar patterns observed in other examined DCI grades. Both uniaxial and torsional fatigue tests, conducted on identical geometries but with varying load ratios, demonstrate the presence of mean stress sensitivity under both loading conditions. This finding emphasizes the importance of incorporating mean stress effects for both mode I and mode III into an appropriate multiaxial fatigue criterion.

Furthermore, Fig. 5d displays the distinct notch sensitivity observed for axial and torsional loadings. The disparity between the fatigue strengths of plain and notched specimens is strongly associated with the type of loading applied. This difference is considerably smaller for torsional loading, where the fatigue strengths of the two geometries coincide, indicating reduced notch sensitivity. The overlap can be elucidated by referring to Fig. 5a, which reveals the impact of pores on the fatigue strengths of unnotched specimens. The varying degrees of notch sensitivity can be attributed to the differing sizes of SED control radii, as proposed by Berto et al. [30].

The experimental evidence presented in Fig. 5 offers insights into the various factors influencing the multiaxial fatigue behavior of DCIs. These factors have been integrated into the proposed multiaxial criterion, which will be elucidated in the subsequent discussion.

4. Multiaxial fatigue criterion

The proposed approach utilizes a strain energy density (SED)-based criterion to assess the fatigue failure of a component. The underlying assumption of this criterion is that fatigue failure occurs when the SED, averaged over a control volume, exceeds a critical value, denoted as W_c. This critical value is typically determined by conducting tests on plain specimens and varies depending on whether the loading is axial (mode I) or torsional (mode III):

$$\overline{W}_{1,\text{plain}} = \frac{1}{2E}\sigma_{a,\text{plain}}^2; \qquad \overline{W}_{3,plain} = \frac{1}{2G}\tau_{a,\text{plain}}^2 \qquad\qquad (5)$$

where $\sigma_{a,\text{plain}}$ and $\tau_{a,\text{plain}}$ are the fatigue strengths, at a given number of cycles to failure, of plain specimens tested under axial and torsional loading, respectively. E is the elastic (Young) modulus and G is the shear modulus. This approach is supposed to work well for the HSi grade, where shrinkage pores are homogeneously distributed within the material. Nevertheless, as already explained, fatigue failure in the GJS-600 and GJS-400 grades is triggered by different features, depending on the specimen's geometry. Therefore, in order to obtain reliable predictions, the critical SED for mode I and III loadings should be assessed by replacing the plain fatigue strengths with the intrinsic fatigue strengths σ_a^* and τ_a^*, representative of a pore-free material. Summarizing:

$$\begin{cases} \overline{W}_1^* = \frac{1}{2E}\sigma_a^{*\,2}; & \overline{W}_3^* = \frac{1}{2G}\tau_a^{*\,2}; & \text{for the GJS} - 600 \text{ and GJS} - 400 \text{ grades} \\ \overline{W}_1^* = \frac{1}{2E}\sigma_{a,\text{plain}}^2; & \overline{W}_3^* = \frac{1}{2G}\tau_{a,\text{plain}}^2; & \text{for the HSi grade} \end{cases} \qquad (6)$$

4.1 Definition of the intrinsic fatigue strengths and the SED control radius under different loading modes

The procedure used to assess the intrinsic fatigue strengths σ_a^* and τ_a^* is based on the SED local approach and provides the SED control radii R_1 and R_3, for mode I and mode III loadings, respectively. The framework, schematized in Fig. 6 and explained in detail in [58,59] and [60], consists in testing two V-notched axisymmetric specimens with different severities, namely a sharp and a blunt notch. According to the SED local method, the SED is averaged over a control volume Ω_1 or Ω_3, for mode I and mode III loading, respectively (see Fig. 1). The characteristic sizes of these control volumes are the SED control radii R_1 and R_3, which are assumed to be a material property, function of the number of cycles to failure [61,62].
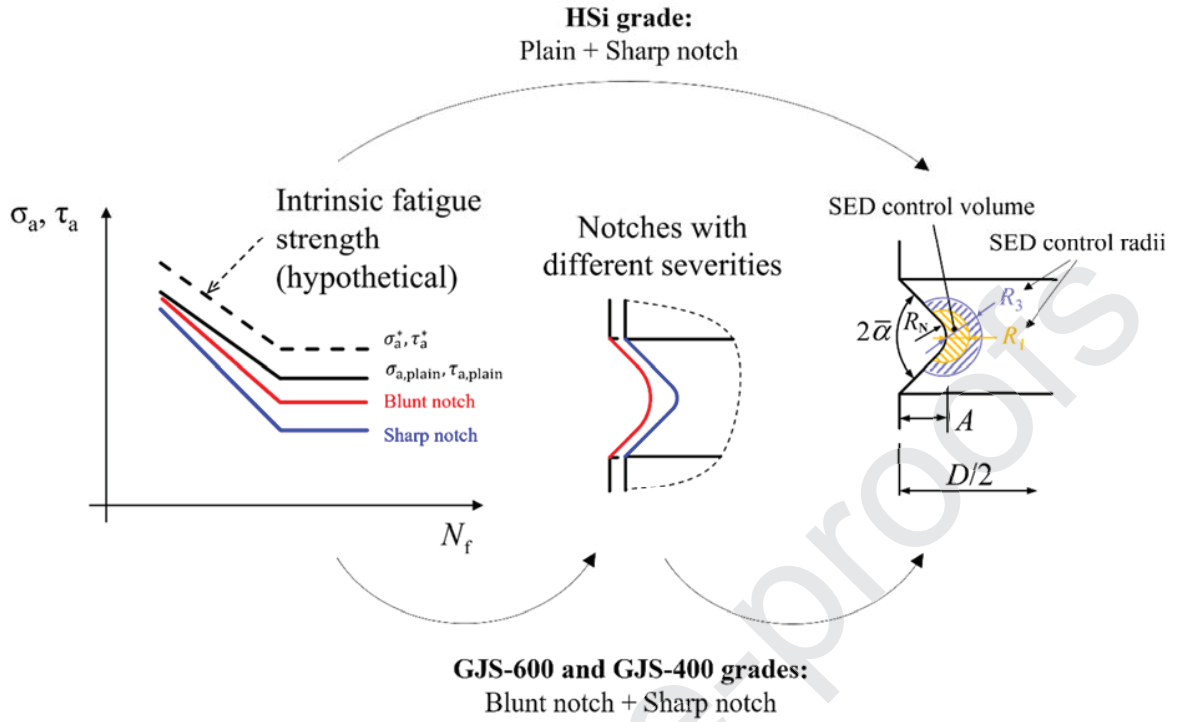
Figure 6. *Schematization of the framework used to determine the mode I and III intrinsic fatigue strengths, and the mode I and III control radii, as function of the DCI grade. The notch depth A is equal to 0.3 D/2 for mode I loading and 0.25 D/2 for mode III loading.*

In V-notched axisymmetric specimens, Ω_1 and Ω_3 are lenticular areas comprised within a circle of radius $r_0 + R_1$ or $r_0 + R_3$, respectively, and centered on the notch bisector at a distance r_0 from the notch tip, defined as:

$$r_0 = R_N \frac{\pi - 2\bar{\alpha}}{2\pi - 2\bar{\alpha}} \tag{7}$$

where R_N is the notch radius and $2\bar{\alpha}$ is the notch opening angle. In [58–60], we proposed an inverse search procedure of the control radii R_1 and R_3, which takes as input the fatigue strengths of a plain and an optimized V-notched specimen. Given the coherence of microstructural defects leading to fatigue failure in plain and notched specimens made of HSi grade, the procedure for mode I and mode III loading is straightforward:

$$\begin{cases} R_1 = \frac{D}{2} f_{1,inversion}\left(\frac{R_N}{\frac{D}{2}}, \frac{\sigma_{a,plain}}{\sigma_{a,N}}\right); & K_{f,N1} = \frac{\sigma_{a,plain}}{\sigma_{a,N}}; \\ R_3 = \frac{D}{2} f_{3,inversion}\left(\frac{R_N}{\frac{D}{2}}, \frac{\sigma_{a,plain}}{\tau_{a,N}}\right); & K_{f,N3} = \frac{\sigma_{a,plain}}{\tau_{a,N}}; \end{cases} \quad \text{for the HSi grade} \tag{8}$$

Instead, for the GJS-600 and GJS-400 grades, the plain fatigue strength is replaced with the intrinsic fatigue strength, and the inversion functions can be defined as:

$$\begin{cases} R_1 = \dfrac{D}{2} f_{1,inversion}\left(\dfrac{R_N}{\frac{D}{2}}, \dfrac{\sigma_a^*}{\sigma_{N,a}}\right); & K_{f,N1} = \dfrac{\sigma_a^*}{\sigma_{N,a}}; \\[3mm] R_3 = \dfrac{D}{2} f_{3,inversion}\left(\dfrac{R_N}{\frac{D}{2}}, \dfrac{\tau_a^*}{\tau_{N,a}}\right); & K_{f,N3} = \dfrac{\tau_a^*}{\tau_{N,a}}; \end{cases} \qquad \text{for the GJS} - 600 \text{ and GJS} - 400 \text{ grades} \qquad (9)$$

Where D is the external diameter of the V-notched specimen, $\sigma_{a,N}$ and $\tau_{a,N}$ are the V-notched specimen fatigue strengths, $K_{f,N1}$ and $K_{f,N3}$ are the mode I and mode III notch fatigue stress concentration factors. Basically, the control radii are defined as a function of the specimen geometry, the intrinsic fatigue strengths, and finite element-based inversion functions. Nevertheless, σ_a^* and τ_a^* are not known a priori, thus making the problem unsolvable. This drawback can be bypassed by testing two V-notched specimens with different severities, as schematized in Fig. 6, namely specimens (c) and (f) for mode I loading, and specimens (d) and (g) for mode III loading. The main assumption of the SED-based approaches states that the control radii are material properties, therefore, they must be the same if assessed by testing a sharp or a blunt V-notched specimen. Consequently, the following equations can be written:

$$\begin{cases} R_1 = \dfrac{D_{sharp}}{2} f_{1,inversion}\left(\dfrac{R_{N,sharp}}{D_{sharp}/2}, \dfrac{\sigma_a^*}{\sigma_{sharp,a}}\right) = \dfrac{D_{blunt}}{2} f_{1,inversion}\left(\dfrac{R_{N,blunt}}{D_{blunt}/2}, \dfrac{\sigma_a^*}{\sigma_{blunt,a}}\right) \\[3mm] R_3 = \dfrac{D_{sharp}}{2} f_{3,inversion}\left(\dfrac{R_{N,sharp}}{D_{sharp}/2}, \dfrac{\tau_a^*}{\tau_{sharp,a}}\right) = \dfrac{D_{blunt}}{2} f_{3,inversion}\left(\dfrac{R_{N,blunt}}{D_{blunt}/2}, \dfrac{\tau_a^*}{\tau_{blunt,a}}\right) \end{cases} \qquad (10)$$

In this way, the intrinsic fatigue strengths σ_a^* and τ_a^* can be assessed by adopting an iterative root search algorithm of Eq. (10). Finally, the control radii can be evaluated according to Eq. (9), utilizing the data related to the sharp V-notched specimen. Unfortunately, no blunt V-notches were produced in the GJS-400 grade, thus making the inversion from double notch unfeasible. Therefore, the intrinsic strengths were evaluated by rescaling the plain fatigue strengths with the well-known Murakami $\sqrt{area}$ formula [63]:

$$\begin{cases} \sigma_a^* = \sigma_{a,plain}\left(\dfrac{d_{F,pore}}{d_{F,nodule}}\right)^{1/6} \\[3mm] \tau_a^* = \tau_{a,plain}\left(\dfrac{d_{F,pore}}{d_{F,nodule}}\right)^{1/6} \end{cases} \qquad (11)$$

where $d_{F,nodule}$ is the mean maximum Feret diameter of the graphite nodules, set equal to 52.5 μm according to [64], and $d_{F,pore}$ is the maximum Feret diameter of the pore expected to be found in the plain specimens, set equal to 1350 μm according to [46], as evidenced by the fracture surface shown in Fig. 5a. Then, the SED control radii were evaluated according to Eq. (9) and using the sharp V-notch data. The values of σ_a^*, τ_a^*, R_1 and R_3, assessed for all the investigated materials, are shown in Fig. 7 as function of the number of cycles to failure.
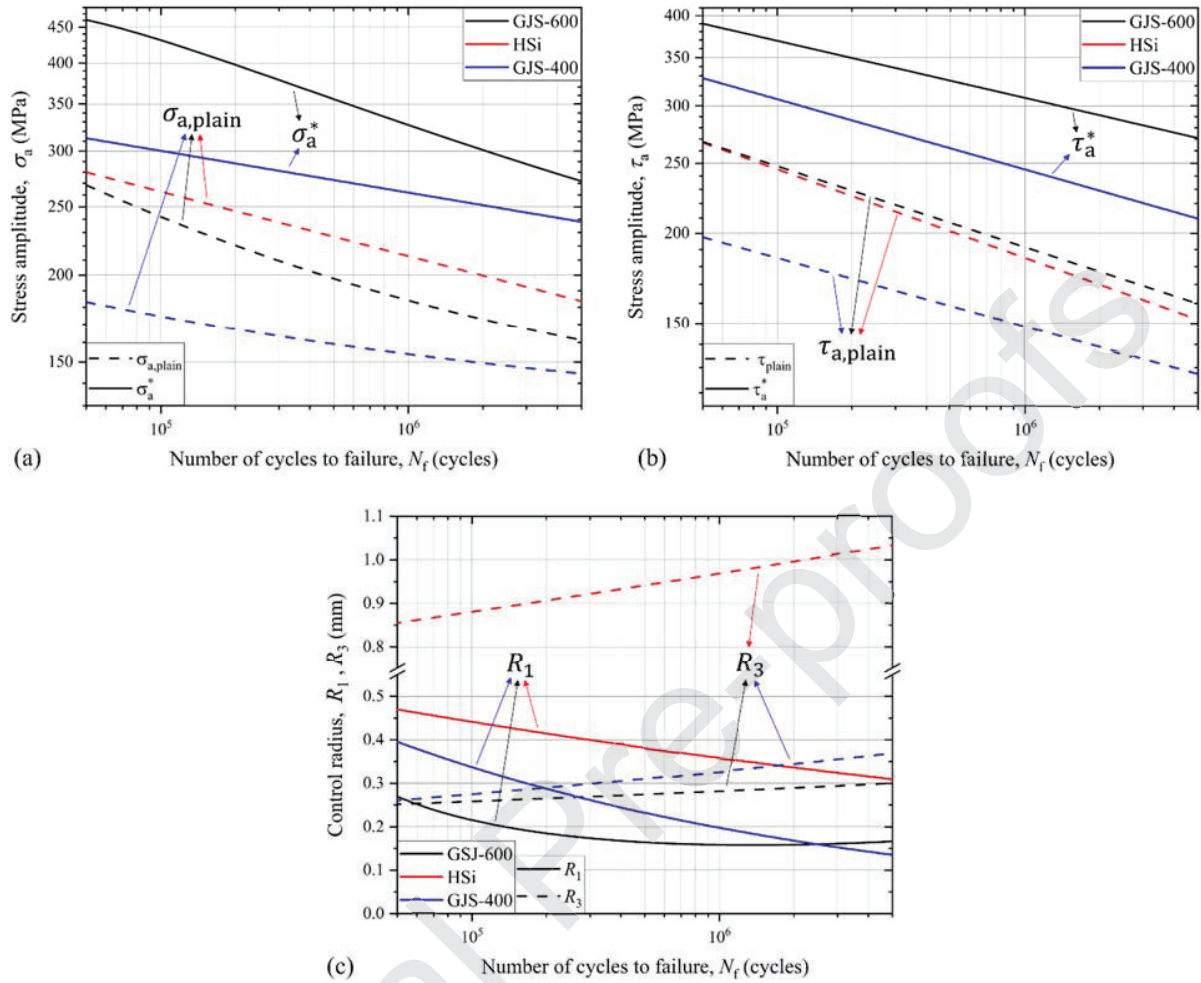
Figure 7. *(a) Mode I plain and intrinsic fatigue strengths, (b) mode III plain and intrinsic fatigue strengths, and (c) mode I and III control radii, as function of the number of cycles to failure N_f, for all the investigated materials.*

As already explained, no intrinsic fatigue strengths were calculated for the HSi grade. Another important consideration regards the assessed intrinsic fatigue strengths of the GJS-600 and GJS-400 grades. In fact, they are in good agreement with the fatigue strengths predicted by Vaara et al. in [65] and the experimental fatigue strengths reported in [66–69]. The reason why they're in agreement is that the reference fatigue strengths above mentioned are obtained for small ductile cast iron casts, which generally don't display any shrinkage porosity.

4.2 Basic formulation of the criterion

Multiaxial (axial + torsional) fatigue tests can be defined through four main parameters, namely the applied axial stress amplitude σ_a, the multiaxiality ratio $\lambda = \tau_a/\sigma_a$ (where τ_a is the applied shear stress amplitude), the stress ratio $R = \sigma_{min}/\sigma_{max}$ (where σ_{min} and σ_{max} are the minimum and maximum axial stress values) and the phase angle φ, which is the shift angle between the sinusoidal axial and torsional loading. Therefore,

a multiaxial fatigue criterion should account for all the above-mentioned parameters. In this work only cyclic loadings at constant frequency are considered. The simple formulation of the criterion we propose is:

$$\sigma_a{}^2 \cdot \overline{W}_{1,U} + (\lambda\,\sigma_a)^2 \cdot \overline{W}_{3,U} = (1 - f)\,\overline{W}_1^* + f\,\overline{W}_3^* \tag{12}$$

where σ_a is the stress amplitude to be predicted. $\overline{W}_{1,U}$ and $\overline{W}_{3,U}$ are the SED values for unitary applied axial or shear stress. Their values depend both on the investigated geometry and the material, thus the control radii, and are calculated as explained in the following. Given the investigated specimen geometry, parametric finite element simulations are carried out by varying the control radius (R_1 for axial loading and R_3 for torsional loading), applying a nominal unitary axial or shear stress, and then assessing the corresponding SED value averaged over the control volume, which is equal to $\overline{W}_{1,U}$ or $\overline{W}_{3,U}$, depending on the applied load. The control volume is placed as schematized in Fig. 1. The unit of measure of the unitary SEDs is mJ/(mm³ MPa²). It should also be noted that $\overline{W}_{1,U}$ and $\overline{W}_{3,U}$ are functions of R_1 and R_3, which are functions of the number of cycles to failure, but material dependent. Therefore, in Eq. (12), $\overline{W}_{1,U}$ and $\overline{W}_{3,U}$ are interpolated according to the proper control radii, depending on the considered number of cycles to failure. f is a modulating function we propose, defined as:

$$f = \left(\frac{1}{2} + \frac{ArcTan(\lambda - \lambda_{th})}{\pi}\right); \quad \lambda_{th} = 15 \tag{13}$$

λ_{th} is a threshold value that indicated the transition from mode I to mode III dominated failure. The limiting cases are $\lambda = 0$, which represent a pure axial loading, and $\lambda = \infty$, which represent a pure torsional loading. It reasonable to think that the higher λ, the lower the influence of the axial stress on the fatigue properties, thus leading to mode III dominated failure. This is confirmed by Fig. 8, where some experimental fatigue data are plotted in terms of equivalent SED. It can be observed that axial and multiaxial fatigue data lie in the vicinity of the line defining the mode I critical SED $\overline{W}_1^*$. Instead, torsional fatigue data lie in the vicinity on the line defining the mode III critical SED $\overline{W}_3^*$. This evidences how multiaxial fatigue failures, at least for the investigated values of λ, are mode I-nominated, while mode III-dominated failures are encountered only when the shear stress component is very high, for instance under pure torsional fatigue.

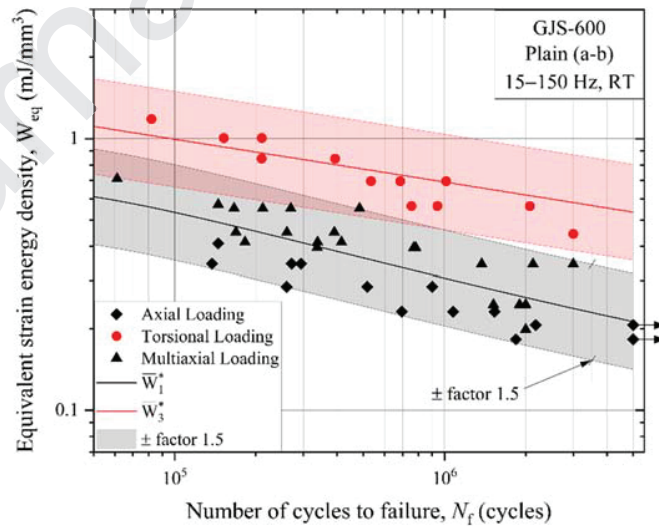**Figure 8.** *Experimental data (data points) represented by means of an equivalent strain energy density (solid lines), versus the critical SEDs $\overline{W}_1^*$ and $\overline{W}_3^*$, as function of the number of cycles to failure N_f. The*

colored bands represent a factor equal to ± 1.5. Axial and multiaxial fatigue failures are mode I-dominated. Torsional fatigue failures are mode III-dominated.

In this work, we set $\lambda_{th} = 15$, which is an extremely high value for normal multiaxial conditions, thus assuming that, inasmuch an axial stress component is present, the fatigue failure is mode I dominated. Basically, $f = 0$ when $\lambda \ll \lambda_{th}$ (axial and multiaxial tests) and $f = 1$ when $\lambda \gg \lambda_{th}$ (torsional tests). The validity of the assumed value of λ_{th} is confirmed by the experimental data used for the model validation, as it will be shown in the following. Nevertheless, the proper value could be set only after a specific experimental campaign. In any case, for a safe design, a worst-case condition, represented by a mode-I dominated failure, can always be considered, thus being conservative in the fatigue predictions.

The proposed criterion can be subdivided into two parts. The left-hand side represents the energy associated to the loads applied to the tested specimen. The stress amplitude to be predicted σ_a scales with the power 2, as the SED can be represented as a stress elevated to the power 2. Since both axial and torsional loads are applied simultaneously, the corresponding SEDs are simply summed. The right-hand side, instead, represents the critical SED leading to fatigue failure. Solving Eq. (12) for σ_a allows to assess the fatigue strength of the investigated component. Nevertheless, the simplified formulation reported in Eq. (12) accounts neither for the mean stress effect, related to the stress ratio R, nor for the phase effect. These effects will be incorporated to the criterion in the following.

4.3 Mean stress effect

The effect of the mean stress, and thus the influence of the load ratio R, is accounted according to Benedetti et al. [37]. In essence, the amplitude and the maximum value of the average SED are incorporated into the following Walker-like equation to express an equivalent SED:

$$
\begin{cases}
\overline{W}_{1,eq} = (\sigma_a{}^\alpha (\sigma_{max})^{1-\alpha})^2 \overline{W}_{1,U} = \left(\sigma_a{}^\alpha \left(\frac{2\,\sigma_a}{1-R} \right)^{1-\alpha} \right)^2 \overline{W}_{1,U} \\[3mm]
\overline{W}_{3,eq} = (\tau_a{}^\beta (\tau_{max})^{1-\beta})^2 \overline{W}_{3,U} =
\begin{cases}
\left((\lambda\,\sigma_a)^\beta \left(\frac{2\,\lambda\,\sigma_a}{1-R} \right)^{1-\beta} \right)^2 \overline{W}_{3,U} & if \quad 0 \le \lambda < \infty \\[3mm]
\left((\tau_a)^\beta \left(\frac{2\,\tau_a}{1-R} \right)^{1-\beta} \right)^2 \overline{W}_{3,U} & if \quad \lambda = \infty
\end{cases}
\end{cases}
\tag{14}
$$

where σ_a or τ_a are the axial and torsional stress amplitudes, σ_{max} or τ_{max} the maximum axial and torsional stresses. α and β are material-dependent parameters that can be experimentally assessed. In this work, the same load ratio R is considered for mode I and mode III loading. Nevertheless, the criterion is still valid if R takes different values for the axial and torsional loadings. It must be underlined that in [37] the equivalent SED is defined in terms of range, and therefore by adopting a notation based on the stress range. In the present work, we generalize every formulation by using the stress amplitude. Nevertheless, if the whole criterion was based on the stress range, the predictions would be the same, as a factor 2 would be introduced in both parts of the equation. The calibration of α and β is carried out by testing plain or V-notched specimens under axial and torsional loading, with a stress ratio R ≥ 0. The obtained fatigue curves are substituted in Eq. (14), in terms of σ_a, τ_a, σ_{max} and τ_{max}, as function of the number of cycles to failure. Then, by solving $\overline{W}_{1,eq} = \overline{W}_1^*$ and $\overline{W}_{3,eq} = \overline{W}_3^*$, the coefficient α and β can be easily assessed. The obtained results are shown in Fig. 9, for all the investigated materials. The lower α and β, the higher the influence of the mean stress on the fatigue properties. Interestingly, the most detrimental effect of mean stresses is

found for the GJS-600 grade. This material is distinguished by a fully pearlitic matrix, which makes the material more brittle in contrast to the other grades under investigation, which possess a ferritic matrix. Consequently, it appears that the impact of mean stresses is amplified as the material becomes more brittle.
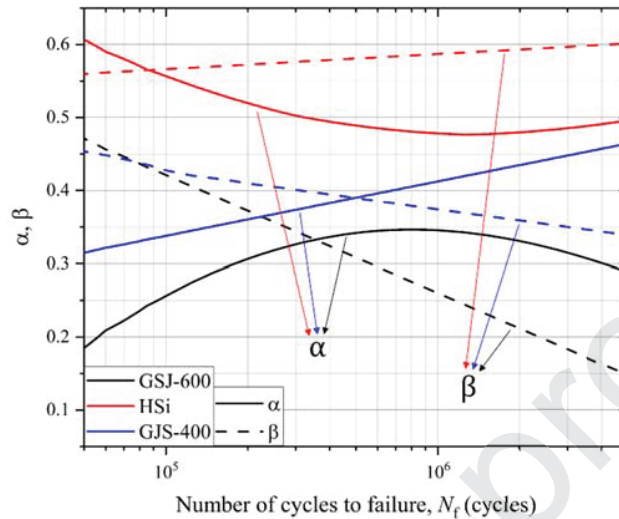
Figure 9. *Material-dependent coefficients α and β, representing the mode I and III mean stress effect, as function of the number of cycles to failure N_f, for all the investigated materials.*

4.4 Phase effect

As evidenced in Fig. 5, a systematic increase in the fatigue strength is observed when out-of-phase loadings are applied to both plain and notched specimens, thus suggesting that the phase effect should be incorporated into the multiaxial fatigue criterion. Moreover, as widely discussed in the introduction, fatigue cracks in DCIs generally nucleate on the planes subjected to the maximum normal stress component. This behavior is evidenced in Fig. 10, which shows fatigue cracks in plain specimens made of DCI GJS-600, subjected different loading conditions. Clearly, in axial, torsional and in-phase multiaxial loading tests, fatigue cracks propagated along the plane subjected to the maximum principal stress.
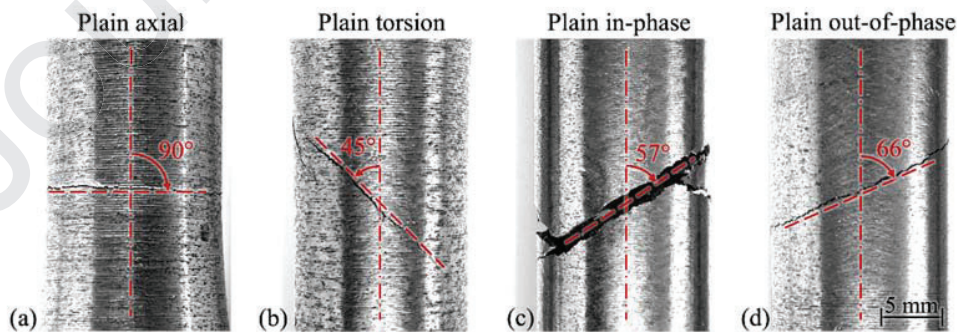
Figure 10. *Fatigue cracks in specimens made of DCI GJS-660, subjected to different loading conditions: (a) axial loading R = -1, (b) torsional loading R = -1, (c) in-phase multiaxial loading λ = 1, R = −1, φ =*

20

0°, (d) (c) out-of-phase multiaxial loading λ = 1, R = −1, φ = 90°. In (a-c), the fatigue cracks propagated along the plane subjected to the maximum principal stress. This picture is a reproduction taken from [2].

To capture the brittle behavior displayed by DCI, we assume that the fatigue damage is linked to the SED peak experienced by the control volume during each loading cycle. If we consider the following time-varying biaxial stress state, produced by a combination of axial and torsional loadings, as shown in Fig. 11a:

$$\begin{pmatrix} \sigma_a \, Sin(\theta) & \tau_a \, Sin(\theta + \varphi) \\ \tau_a \, Sin(\theta + \varphi) & 0 \end{pmatrix} \tag{15}$$

where $0 < \theta < 2\pi$ is the angle representing the cycle evolution, σ_a and τ_a are generic stress amplitude and φ is the phase shift angle between the axial and the torsional loading. The total strain energy density can be expressed as a sum of the mode I and mode III SEDs:

$$W_{\text{tot}} = \frac{(\sigma_a \, Sin(\theta))^2}{2 \, E} + \frac{(\tau_a \, Sin(\theta+\varphi))^2}{2 \, G} = \frac{(\sigma_a \, Sin(\theta))^2}{2 \, E} + \frac{(\lambda \, \sigma_a \, Sin(\theta+\varphi))^2}{2 \, \frac{E}{2(1+\nu)}} \tag{16}$$

The total SED is shown in Fig. 11b for different values of the phase angle φ, and unitary applied axial and shear stress amplitudes.
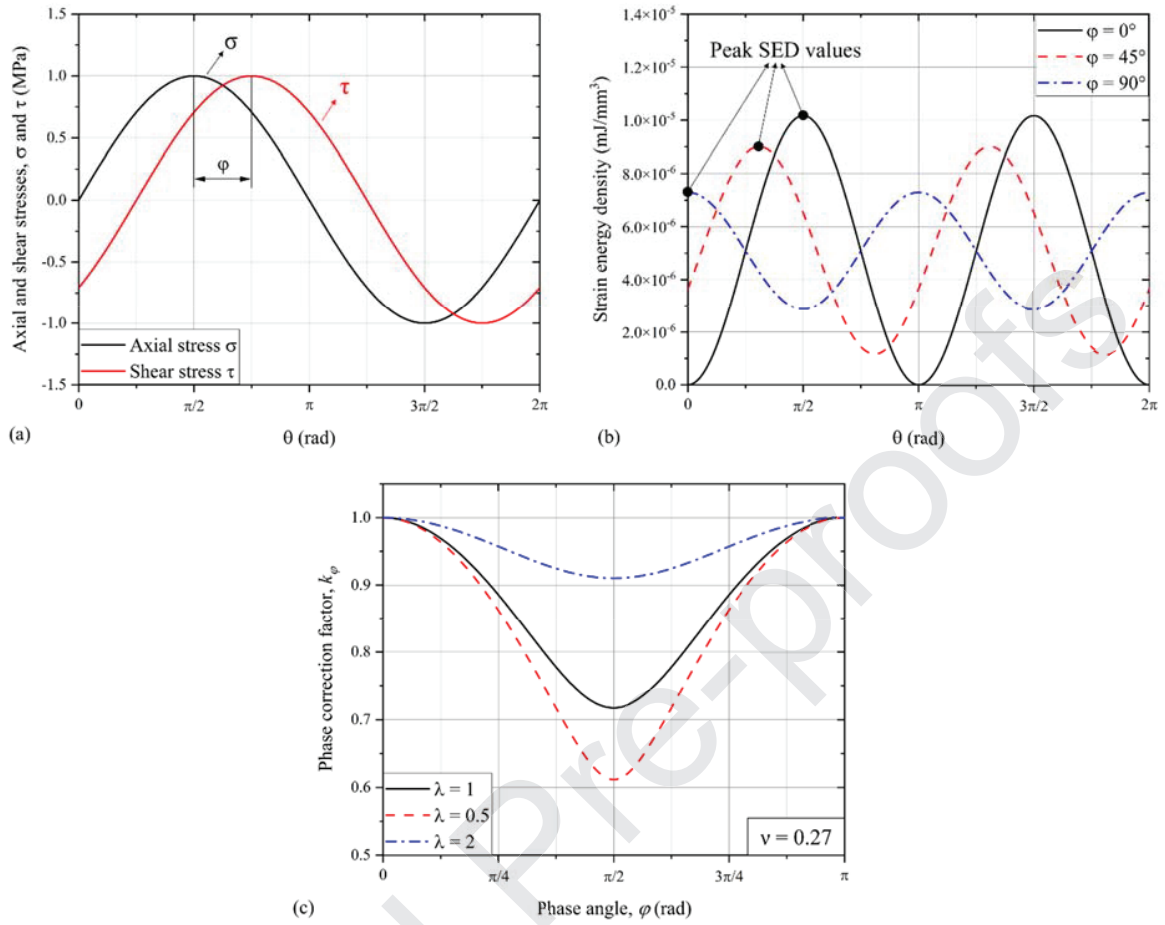
Figure 11. *(a) Axial and shear stresses in a general out-of-phase loading condition, (b) corresponding strain energy densities evolution during the loading cycle, for different phase angle φ values. (c) Phase correction factor k_φ as a function of phase angle φ and biaxiality ratio λ (Eq. (18)).*

It can be demonstrated that the SED peak reached in the loading cycle is given by:

$$W_{\text{tot,peak}} = \frac{\sigma_a^2 \left(1 + 2\,\lambda^2\,(1+\nu) + \sqrt{1 + 4\,\lambda^4\,(1+\nu)^2 + 4\,\lambda^2\,(1+\nu)\,Cos(2\,\varphi)} \right)}{4\,E} \tag{17}$$

To extend the validity of the criterion reported in Eq. (12), which basically assumes the mode I and III SED peaks to be achieved simultaneously ($\varphi = 0°$), we propose to introduce the following phase correction factor k_φ as the ratio between $W_{\text{tot,peak}}$ calculated for a generic phase angle φ, and $W_{\text{tot,peak}}$ calculated for $\varphi=0°$:

$$k_\varphi = \frac{1 + 2\,\lambda^2\,(1+\nu) + \sqrt{1 + 4\,\lambda^4\,(1+\nu)^2 + 4\,\lambda^2\,(1+\nu)\,Cos(2\,\varphi)}}{2 + 4\,\lambda^2\,(1+\nu)} \tag{18}$$

Figure 11c shows how k_φ varies as a function of φ and λ. It can be noted that for out-phase loading k_φ is lower than 1. Moreover, the higher the biaxiality ratio λ, the closer k_φ is to 1, thus the smaller the phase effect. k_φ can be used to account for the experimentally observed phase strengthening effect. The proposed approach assumes uniform sensitivity to nonproportionality across different materials. However, it is important to note that the study exclusively focuses on DCI grades, known for their brittle behavior and

22

exhibiting the same strengthening behavior when subjected to out-of-phase loadings. As a result, it may be reasonable to extrapolate the effect of non-proportional loadings to all DCI grades studied. Further investigations are necessary to evaluate the phase sensitivity of other material classes.

4.5 Complete formulation of the criterion

The complete formulation of the criterion, which includes both the mean stress and the phase effects, is formulated as following:

$$
\begin{cases}
k_\varphi \left(\overline{W}_{1,eq} + \overline{W}_{3,eq} \right) = (1 - f)\, \overline{W}_1^* + f\, \overline{W}_3^* \\[2mm]
\overline{W}_{1,eq} = \left(\sigma_a{}^\alpha \left(\frac{2\,\sigma_a}{1-R} \right)^{1-\alpha} \right)^2 \overline{W}_{1,U} \\[2mm]
\overline{W}_{3,eq} =
\begin{cases}
\left((\lambda\,\sigma_a)^\beta \left(\frac{2\,\lambda\,\sigma_a}{1-R} \right)^{1-\beta} \right)^2 \overline{W}_{3,U} & if \quad 0 \le \lambda < \infty \\[3mm]
\left((\tau_a)^\beta \left(\frac{2\,\tau_a}{1-R} \right)^{1-\beta} \right)^2 \overline{W}_{3,U} & if \quad \lambda = \infty
\end{cases}
\end{cases}
\tag{19}
$$

The SED associated to the load application, thus $\overline{W}_{1,eq} + \overline{W}_{3,eq}$, is rescaled according to the strengthening factor k_φ, defined in Eq. (18), as a function of the phase angle φ and the multiaxiality ratio λ. The different notch sensitivity observed under mode I and mode III loading is accounted by using different control radii, namely R_1 and R_3, for the assessment of $\overline{W}_{1,U}$ and $\overline{W}_{3,U}$. We want to remark that the parameters assessed as function of the number of cycles to failure N_f are: $\overline{W}_1^*$ and $\overline{W}_3^*$, $\overline{W}_{1,U}$ and $\overline{W}_{3,U}$ (which depend on R_1 and R_3, again assessed as function of N_f), α and β. The stress amplitude σ_a is therefore predicted as function of N_f. All the other parameters, instead, regard the loading conditions.

Axial and multiaxial tests are referred to the axial stress amplitude σ_a, which is directly linked to the shear stress amplitude τ_a through the multiaxiality ratio λ. When purely torsional tests are considered, λ becomes equal to ∞ and the previous approach does not work anymore. Therefore, for torsional tests, fatigue data and predictions are directly referred to τ_a. This is valid for every tested geometry and material and for the criterion formulations presented in the following.

The criterion can be easily extended to plain specimens, considering that the concept of critical volume loses its meaning here and that SED values are defined according to Eq. (5). Since, in plain specimens, fatigue failures are always triggered by shrinkage pores, the predicted fatigue strengths must be rescaled according to the Murakami-like formula proposed in [63]. Nevertheless, this procedure is not adopted for the HSi grade, as shrinkage pores are considered as an intrinsic feature of the material. Therefore, the criterion is formulated, for plain specimens, as:

$$
\begin{cases}
k_\varphi \left(\frac{1}{2\,E} \left(\sigma_a{}^\alpha \left(\frac{2\,\sigma_a}{1-R} \right)^{1-\alpha} \right)^2 + \frac{1}{2\,G} \left((\lambda\,\sigma_a)^\beta \left(\frac{2\,\lambda\,\sigma_a}{1-R} \right)^{1-\beta} \right)^2 \right) = (1-f)\, \overline{W}_1^* + f\, \overline{W}_3^* \\[3mm]
\sigma_{a,real} = \sigma_a \left(\frac{d_{F,nodule}}{d_{F,pore}} \right)^{1/6} ; \qquad \text{for the GJS} - 600 \text{ and GJS} - 400 \text{ grades} \\[3mm]
\sigma_{a,real} = \sigma_a ; \qquad \text{for the HSi grade}
\end{cases}
\tag{20}
$$

To summarize, the calibration of the proposed multiaxial fatigue criterion requires 6 different fatigue curves, and it is material dependent. The required curves are reported in Table 3, as function of the investigated material.

Table 3. Required S-N fatigue curves for the criterion calibration, as function of the investigated DCI grade.

GJS-600 and GJS-400		HSi	
Geometry	**Loading mode**	**Geometry**	**Loading mode**
Sharp V-notch	Axial, R = -1	Sharp V-notch	Axial, R = -1
Sharp V-notch	Torsion, R = -1	Sharp V-notch	Torsion, R = -1
Blunt V-notch	Axial, R = -1	Plain	Axial, R = -1
Blunt V-notch	Torsion, R = -1	Plain	Torsion, R = -1
Generic V-notch	Axial, R ≥ 0	Generic V-notch	Axial, R ≥ 0
Generic V-notch	Torsion, R ≥ 0	Generic V-notch	Torsion, R ≥ 0

The calibration procedure is schematized in the flowchart shown in Fig. 12.
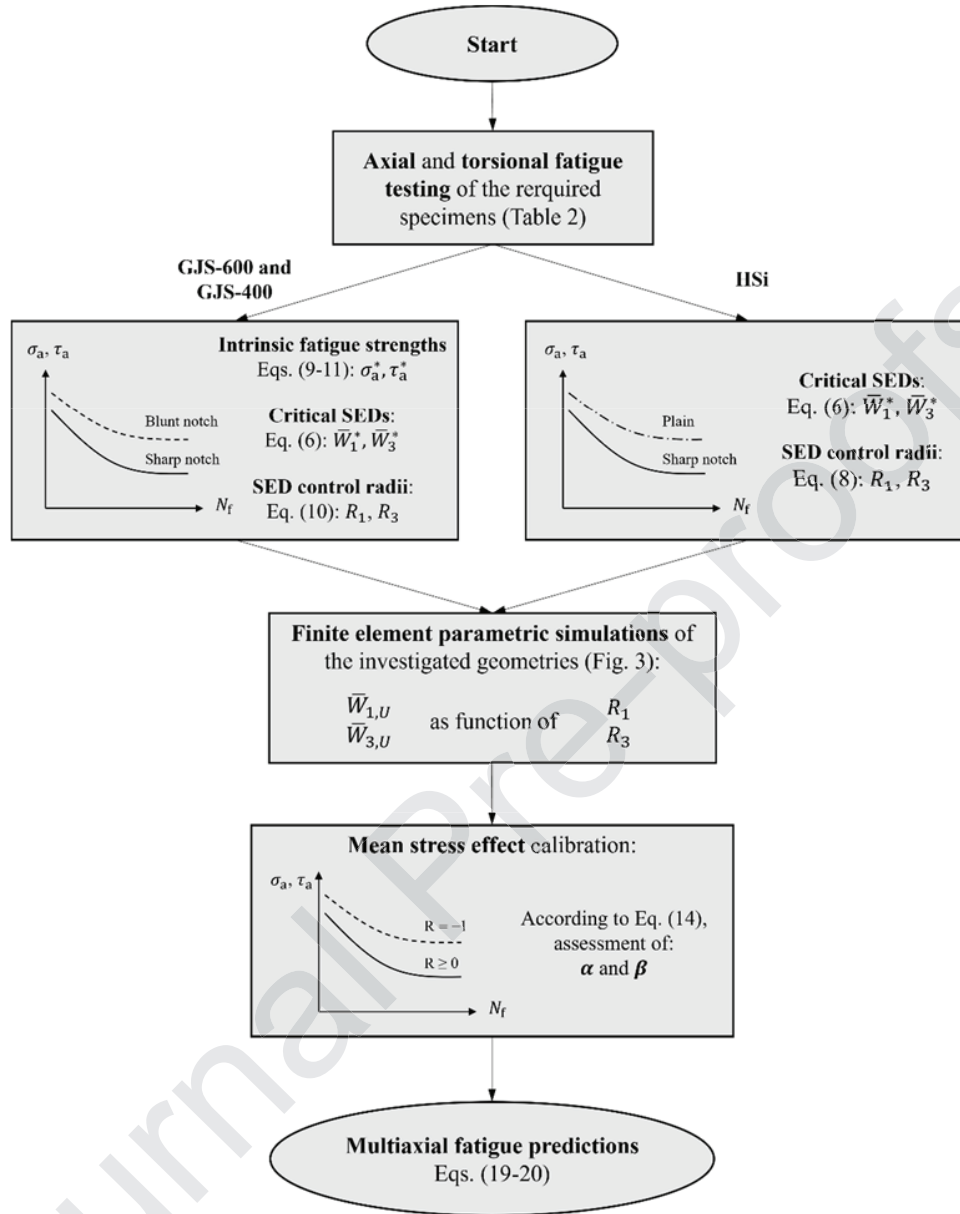
Figure 12. *Flowchart schematizing the calibration of the multiaxial fatigue criterion, depending on the specific investigated DCI grade.*

4.6 Simplified formulation of the criterion

To reduce the number of required fatigue curves for the criterion calibration, a simplified version of the multiaxial fatigue criterion can be formulated. According to Smith, Watson and Topper [70,71], the Walker-like formulation presented in Eq. (14) can be modified by imposing $\alpha = \beta = 0.5$, thus obtaining a simplified version of the equivalent SEDs:

$$\begin{cases} \overline{W}_{1,eq} = (\sigma_a^{0.5}(\sigma_{max})^{0.5})^2 \overline{W}_{1,U} = \sigma_a \left(\frac{2\,\sigma_a}{1-R}\right) \overline{W}_{1,U} \\ \overline{W}_{3,eq} = (\tau_a^{0.5}(\tau_{max})^{0.5})^2 \overline{W}_{3,U} = \lambda\,\sigma_a \left(\frac{2\,\lambda\,\sigma_a}{1-R}\right) \overline{W}_{3,U} \end{cases} \tag{21}$$

Therefore, the simplified multiaxial fatigue criterion, for notched specimens, becomes:

$$k_\varphi \left(\sigma_a \left(\frac{2\,\sigma_a}{1-R}\right) \overline{W}_{1,U} + \lambda\,\sigma_a \left(\frac{2\,\lambda\,\sigma_a}{1-R}\right) \overline{W}_{3,U} \right) = (1-f)\,\overline{W}_1^* + f\,\overline{W}_3^* \tag{22}$$

While, for plain specimens, it can be formulated as:

$$\begin{cases} k_\varphi \left(\frac{1}{2\,E} \left(\sigma_a \left(\frac{2\,\sigma_a}{1-R}\right) \right) + \frac{1}{2\,G} \left(\lambda\,\sigma_a \left(\frac{2\,\lambda\,\sigma_a}{1-R}\right) \right) \right) = (1-f)\,\overline{W}_1^* + f\,\overline{W}_3^* \\ \sigma_{a,real} = \sigma_a \left(\frac{d_{F,nodule}}{d_{F,pore}}\right)^{1/6}; \qquad \text{for the GJS} - 600 \text{ and GJS} - 400 \text{ grades} \\ \sigma_{a,real} = \sigma_a; \qquad \text{for the HSi grade} \end{cases} \tag{23}$$

This simplified formulation represents an alternative to the complete formulation. The advantage is that the parameters α and β do not need to be calibrated anymore. This translates in a loss of accuracy, as it will be shown in the following. Nevertheless, the committed errors are still reasonably low.

4.7 Important remarks on the proposed criterion

To better clarify the proposed criterion before proceeding to the validation section, some remarks are necessary. The criterion aims to predict the stress amplitude that leads to fatigue failure based on the number of cycles to failure and the multiaxial fatigue parameters, namely λ, R, and φ. To make accurate predictions, it is essential to calibrate the criterion on the specific material under investigation, as explained in detail in Section 4 and illustrated in the flowchart depicted in Fig. 12. The material-dependent properties/parameters obtained from the calibration are:

- the critical SEDs $\overline{W}_1^*$ and $\overline{W}_3^*$;
- the SED control radii R_1 and R_3;
- the parameters α and β, accounting for the mean stress effect.

which describe the behavior of the investigated material under multiaxial fatigue. Therefore, any variation in the microstructure directly translates in a variation of these properties/parameters.

There is an important point to note about the type of predictions that the criterion produces. As it stands, the criterion offers forecasts in terms of stress amplitudes, as a function of the number of cycles until failure. However, it is possible to obtain predictions in terms of fatigue life as a function of the applied stress amplitude with ease, as discussed in Section 5. In essence, the criterion produces S-N fatigue curves, which can be conveniently interpolated by setting the applied stress amplitude. This allows for the prediction of the expected number of cycles to failure.

5. Criterion validation on independent multiaxial fatigue data sets

The criterion was validated by means of multiaxial fatigue data obtained by testing different geometries and materials, with different combinations of the main multiaxial fatigue parameters, namely R, λ and φ. It

must be pointed out that the datasets used for the validation are completely independent of those used for the criterion calibration. Indeed, the criterion calibration only requires axial and torsional fatigue tests, and no combinations of these loading modes. The predictions (thick solid lines), obtained by applying the complete criterion formulation, Eqs. (19-20), are compared to the collected multiaxial fatigue experimental data in Fig. 13, where the colored bands represent the 10 % to 90 % failure probability, the thin solid lines represent the 50 % failure probability, and the dots represent the experimental data points.
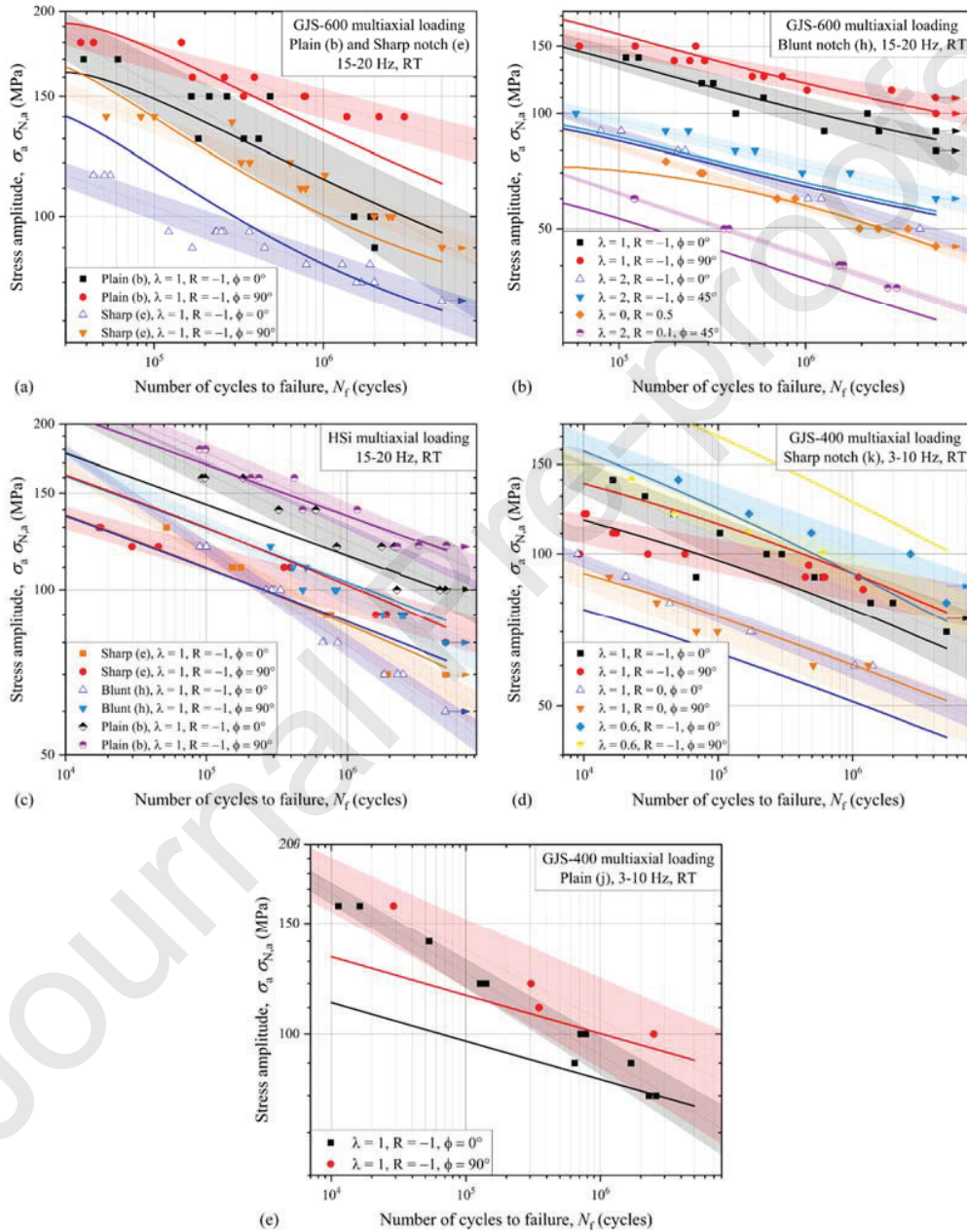

Figure 13. Multiaxial fatigue predictions (solid lines) versus experimental data (data points) as function of the number of cycles to failure N_f, for the (a-b) GJS-600 grade, (c) HSi grade, and (d) GJS-400 grade. The thin lines represent the experimental 50 % failure probability, while the colored bands the 10 to 90 % failure probability.

27

It can be observed that predictions become less accurate when moving towards higher stress amplitudes, thus towards shorter fatigue lives. This loss of accuracy is probably due to the increasing plastic work taking place in the region close to low cycle fatigue regime. In fact, the whole method was developed and applied in elastic conditions. This is a very important advantage, as it greatly simplifies the FE simulations compared to elastic-plastic conditions. The elastic-plastic modeling of real components could be indeed demanding or even unfeasible, especially when designers must deal with components characterized by complex shapes or large dimensions. Nevertheless, predictions are very accurate in the high-cycle fatigue regime, where the plastic work is small or even absent. The fatigue strengths, predictions, according to Eqs. (19-20), and errors at 5×10^6 cycles are reported in Table 4 for all the investigated DCI grades and geometries. The total root mean square (RMS) error, evaluated at 5×10^6 cycles, is 11.02 %.

Table 4. Multiaxial fatigue predictions ($\sigma_{a,pred}$) versus experimental data ($\sigma_{a,exp}$) at $N_f = 5 \times 10^6$ cycles. The committed error is also reported.

	Specimen	Loading conditions	$\sigma_{a,exp}$ @ 5×10^6 cycles (MPa)	$\sigma_{a,pred}$ @ 5×10^6 cycles (MPa)	Error (%)
GJS-600	Plain (b)	λ=1, R=−1, φ=0°	90.62	94.72	4.52
	Plain (b)	λ=1, R=−1, φ=90°	131.29	111.82	-14.83
	Blunt Notch (h)	λ=0, R=0.5	45.30	44.76	-1.19
	Blunt Notch (h)	λ=1, R=−1, φ=0°	81.68	85.58	4.77
	Blunt Notch (h)	λ=1, R=−1, φ=90°	104.54	101.03	-3.36
	Blunt Notch (h)	λ=2, R=−1, φ=0°	48.12	54.44	13.13
	Blunt Notch (h)	λ=2, R=−1, φ=45°	60.63	55.63	-8.25
	Blunt Notch (h)	λ=2, R=0.1, φ=45°	32.53	28.77	-11.56
	Sharp Notch (e)	λ=1, R=−1, φ=0°	73.39	72.65	-1.01

	Sharp Notch (e)	$\lambda=1$, R=-1, $\varphi=90°$	92.98	85.77	-7.75
	RMS error = 8.43 %				
HSi	Plain (b)	$\lambda=1$, R=-1, $\varphi=0°$	101.24	99.60	-1.62
	Plain (b)	$\lambda=1$, R=-1, $\varphi=90°$	114.27	117.59	2.91
	Blunt Notch (h)	$\lambda=1$, R=-1, $\varphi=0°$	59.38	74.46	25.40
	Blunt Notch (h)	$\lambda=1$, R=-1, $\varphi=90°$	80.31	87.91	9.46
	Sharp Notch (e)	$\lambda=1$, R=-1, $\varphi=0°$	65.44	72.27	10.44
	Sharp Notch (e)	$\lambda=1$, R=-1, $\varphi=90°$	86.00	85.32	-0.79
	RMS error = 11.94 %				
GJS-400	Plain (j)	$\lambda=1$, R=-1, $\varphi=0°$	75.44	77.09	2.19
	Plain (j)	$\lambda=1$, R=-1, $\varphi=90°$	88.64	91.00	2.66
	Sharp Notch (k)	$\lambda=1$, R=-1, $\varphi=0°$	69.50	64.88	-6.65
	Sharp Notch (k)	$\lambda=1$, R=-1, $\varphi=90°$	80.70	76.60	-5.08
	Sharp Notch (k)	$\lambda=1$, R=0, $\varphi=0°$	50.23	43.36	-13.68
	Sharp Notch (k)	$\lambda=1$, R=0, $\varphi=90°$	48.95	51.18	4.56

| Sharp Notch (k) | λ=0.6, R=−1, φ=0° | 86.41 | 73.52 | -14.92 |
| Sharp Notch (k) | λ=0.6, R=−1, φ=90° | 78.92 | 101.73 | 28.90 |

RMS error = 12.98 %

Total RMS error @ 5×10⁶ cycles = 11.02 %

The multiaxial fatigue predictions are presented in Fig. 14 also for a fatigue life ranging from 10^4 and 5×10^6 cycles. The results are presented in terms of predicted stress amplitudes versus experimental stress amplitudes, for all the investigated DCI grades and by applying different formulations of the SED-based approach. Fig. 14a refers to the complete formulation of the criterion we propose, explained in Section 4.5 and represented by Eqs. (19-20). Fig. 14b refers to the simplified formulation of the criterion, obtained by imposing $\alpha = \beta = 0.5$, explained in Section 4.6 and represented by Eqs. (22-23). In the end, Fig. 14c refers to the original formulation of the approach, explained in the introduction Section and represented by Eq. (1).

Figure 14. *Multiaxial fatigue predictions in terms of predicted stress amplitude versus experimental stress amplitude for all the investigated DCI grades and different SED-based formulations: (a) complete formulation of the proposed criterion, with the calibrated coefficients α and β, (b) simplified formulation of the proposed criterion, and (c) original formulation, Eq (1).*

The complete criterion formulation offers the most accurate predictions, with a total root-mean-square (RMS) error of 12.2 %. If only tests with non-zero mean stresses are considered the RMS error becomes 11.2 %. If the simplified formulation, Fig 14b, is adopted, the total RMS error slightly increases up to 12.9 %, but the great advantage is that the number of S-N curves required for the criterion calibration decreases to 4. If only tests with non-zero mean stresses are considered the RMS error becomes 10.6 %. It can be observed that the criteria proposed in this work lead to lower errors (comprised in a ± 15 % error band)

30

compared to the original formulation reported in Eq. (1). As mentioned earlier, evaluating predictions based on fatigue life is also essential. To that end, Figure 15 presents the comparison between predicted and experimental fatigue life using various SED-based approaches.
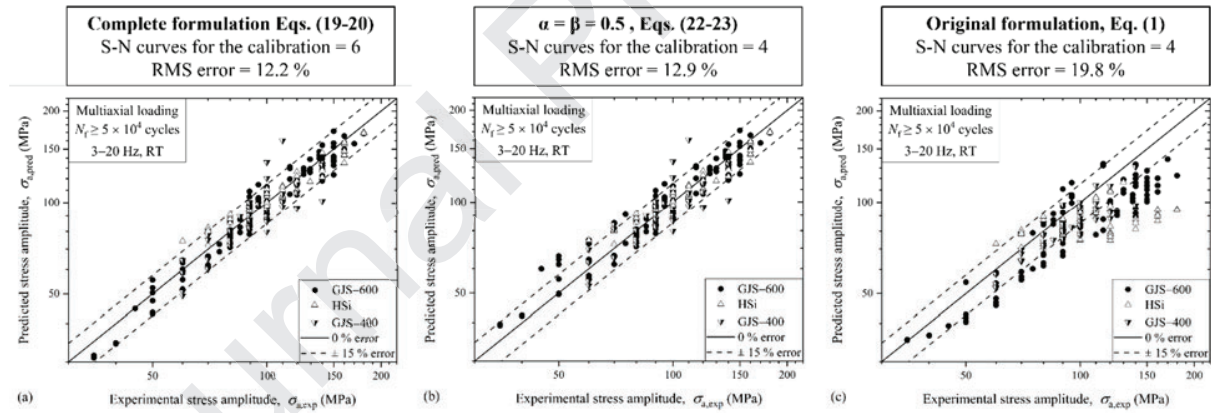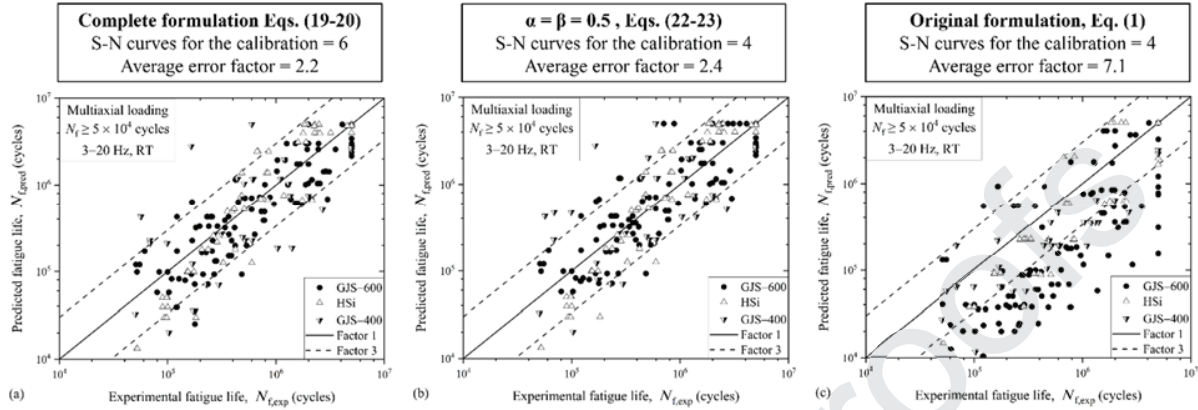

Figure 15. Multiaxial fatigue predictions in terms of predicted fatigue life versus experimental fatigue life for all the investigated DCI grades and different SED-based formulations: (a) complete formulation of the proposed criterion, with the calibrated coefficients α and β, (b) simplified formulation of the proposed criterion, and (c) original formulation, Eq (1).

In this case, the error committed in fatigue live estimations is assessed through an error factor defined as the ratio between the predicted and the experimental fatigue life. The complete formulation of the criterion yields the best predictions, although the simplified formulation shows a low increase in the committed error, as shown in Fig. 14b. It is worth noting that the original formulation, presented in Figs. 14c and 15c, results in a larger committed error than the criterion proposed in this work. However, the predictions are typically conservative, which confirms the high reliability of SED-based approaches. In Fig. 16, the predictions obtained using Eqs. (19-20) of the complete formulation are presented in terms of equivalent strain energy density versus the number of cycles to failure. The experimental stress amplitudes for notched and plain specimens are replaced in Eqs. (19-20) to obtain the data points.
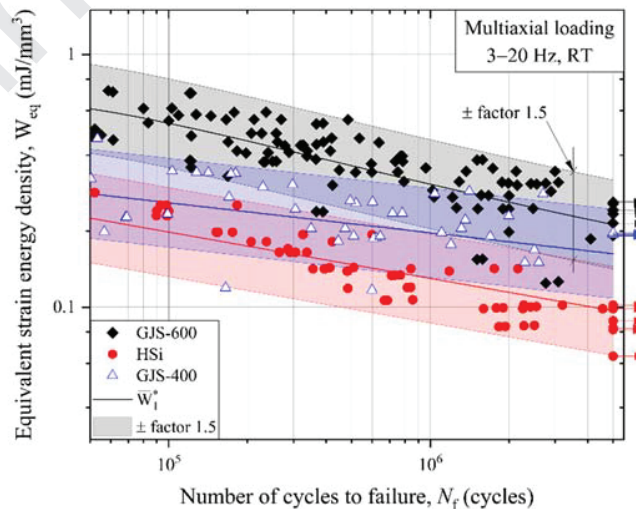
Figure 16. *Experimental data (data points) represented by means of an equivalent strain energy density (solid lines), versus the critical SED* $(1-f)\,\overline{W}_1^* + f\,\overline{W}_3^* \approx \overline{W}_1^*$, *as function of the number of cycles to failure* N_f. *The colored bands represent a factor equal to* ± 1.5. *The calculations were carried out according to the complete formulation of the criterion.*

The colored bands represent the critical SED value used as reference to carry out predictions, namely $(1-f)\,\overline{W}_1^* + f\,\overline{W}_3^* \approx \overline{W}_1^*$, $\pm$ a factor of 1.5, for all the investigated DCI grades. Obviously, since the SED scales with the power 2 of the stress, the committed error is higher than for the stress amplitude predictions. Nevertheless, most of the data points lie close to the mode I critical SED $\overline{W}_1^*$, confirming the hypothesis that multiaxial fatigue failures in DCIs are generally mode I dominated.

5.1 Comparison with critical plane-based approaches

To enhance the comprehension of the effectiveness of the proposed criterion, this section employs a set of multiaxial fatigue data, obtained from testing the GJS-600 grade, to carry out predictions and assess the error involved. This data set has been previously analyzed by Benedetti et al. in [2]. In Table 5, we compare several multiaxial fatigue criteria, including Fatemi-Socie [17], MWCM [72], Carpinteri et al. [8], and Modified SWT [28], to the proposed criterion presented in this study. The notations "3p" and "4p" describe the number of parameters, namely 3 or 4, required for the criterion calibration.

Table 5. Multiaxial fatigue experimental data ($\sigma_{a,exp}$) and predictions ($\sigma_{a,pred}$) carried out by using the proposed SED-based criterion and several critical plane-based criteria. The reported data correspond to a fatigue life of $N_f = 5 \times 10^6$ cycles.

Specimen	Loading condition	$\sigma_{a,exp}$ (MPa)	Method	Proposed criterion		Method	Fatemi-Socie [17]		MWCM [72]		Carpinteri et al. [8]		Modified SWT [28]	
				$\sigma_{a,pred}$ (MPa)	Error (%)		$\sigma_{a,pred}$ (MPa)	Error (%)	$\sigma_{a,pred}$ (MPa)	Error (%)	$\sigma_{a,pred}$ (MPa)	Error (%)	$\sigma_{a,pred}$ (MPa)	Error (%)
Blunt Notch (g)	Torsion R=−1	192.6	Complete Eqs. (22-23)	192.5	-0.05*	3p	226	17.34	-	-	214	11.11	217	12.67
			Simplified Eqs. (25-26)	192.5	-0.05*	3p	226	17.34	-	-	214	11.11	217	12.67
Sharp Notch (e)	$\lambda=1$ R=−1 $\varphi=0°$	73.4	Complete Eqs. (22-23)	72.7	-0.95	3p	72.5	-1.23	61.6	-16.08	74.8	1.91	73.1	-0.41
			Simplified Eqs. (25-26)	72.7	-0.95	4p	61.7	-15.94	-	-	76.9	4.77	65.9	-10.22

Journal Pre-proofs

Sharp Notch (e)	λ=1 R=−1 φ=90°	93	Complete Eqs. (22-23)	85.8	-7.74	3p	92.7	-0.32	60.2	-35.27	82.3	-11.51	91.8	-1.29
			Simplified Eqs. (25-26)	85.8	-7.74	4p	92.6	-0.43	-	-	90.2	-3.01	102	9.68
Blunt Notch (h)	λ=1 R=−1 φ=0°	81.7	Complete Eqs. (22-23)	85.6	4.77	3p	90.6	10.89	88	7.71	90.5	10.77	90.8	11.14
			Simplified Eqs. (25-26)	85.6	4.77	4p	83.2	1.84	-	-	98.5	20.56	91.8	12.36
Blunt Notch (h)	λ=1 R=−1 φ=90°	104.5	Complete Eqs. (22-23)	101.0	-3.35	3p	118	12.92	108	3.35	100	-4.31	118	12.92
			Simplified Eqs. (25-26)	101.0	-3.35	4p	118	12.92	-	-	114	9.09	118	12.92
Sharp Notch 90° (i)	Axial R=0.1	55.1	Complete Eqs. (22-23)	55.1	0*	3p	71.7	30.13	-87.0	-257.89	57	3.45	63.4	15.06
			Simplified Eqs. (25-26)	65.2	18.33	4p	68.3	23.96	-	-	58	-	74.1	34.48
RMS error (%)			Complete Eqs. (22-23)	4.87		3p	15.79		116.69		8.23		10.65	
			Simplified Eqs. (25-26)	9.28		4p	14.13		-		10.63		18.48	

* Fatigue data used for the criterion calibration. This error is not considered in the total RMS error.

The proposed SED-based criterion has demonstrated its effectiveness in providing reliable multiaxial fatigue predictions, as shown by the comparable RMS errors with the well-established Carpinteri et al. criterion [8], which have the advantage of orienting the critical plane according to the material ductility and is therefore able to capture the brittle behavior of DCI. On the contrary, the Fatemi-Socie criterion [17] is affected by slightly higher RMS errors, presumably because it is based on the assumption that the critical plane is the one experiencing the maximum range of shear strain, which is generally valid for ductile materials, such as steel.

To conclude, the proposed criterion offers several advantages. Firstly, the mesh size-sensitivity of the proposed criterion is lower compared to critical plane-based criteria, which requires the assessment of local stress and strain states. The reason is the intrinsic low sensitivity to mesh size of SED-based approaches [30,58]. This attribute enables designers to decrease the computational power required for Finite Element (FE) simulations, making the criterion more cost-effective. Secondly, implementing the proposed SED-based criterion into FE code is straightforward and only requires defining the control volume at the geometrical discontinuity. Finally, the proposed criterion works with scalars instead of tensors, which makes it easier to understand from a conceptual point of view. This significantly increases the potential of applicability of the criterion in the industry.

6. Conclusions

In this work, a novel volumetric SED-based multiaxial fatigue criterion for ductile cast irons was proposed and successfully validated on a large amount of independent experimental data. The main conclusions can be summarized as follows:

1. The criterion accurately assesses the multiaxial fatigue properties of DCI grades with different microstructures, namely fully pearlitic, ferritic-pearlitic and ferritic (high Si content). The effect of the microstructure is incorporated in the critical strain energy densities and the SED control radii R_1 and R_3.
2. The different notch sensitivity under mode I and mode III loadings is accounted by the different sizes of the SED control radii R_1 and R_3.
3. The effect of mean stresses is well assessed by two distinct material-dependent coefficients α and β, for axial and torsional loading, respectively. The use of two distinct coefficients allows the criterion to distinguish between the effect of mean axial stresses and mean shear stresses. Even if a simplified formulation of the criterion is adopted, thus by imposing $\alpha = \beta = 0.5$, the total RMS error slightly increases compared to the complete formulation of the criterion.
4. The effect of out-of-phase loading is accounted by means of a strengthening factor k_φ that predicts the increase of fatigue strengths when out-of-phase loadings are applied.
5. The complete criterion calibration requires a total of 6 fatigue curves:
   a. Blunt V-notches tested under axial and torsional loading, at a stress ratio R = −1;
   b. Blunt V-notches tested under axial and torsional loading, at a stress ratio R = −1;
   c. Generic V-notches tested under axial and torsional loading, at a stress ratio R ≥ 0.
6. If the simplified formulation of the criterion is adopted, the calibration of the coefficients α and β is not necessary, therefore only 4 fatigue curves are required for the criterion calibration.
7. The proposed SED-based criterion provides comparable accuracy to well-established critical plane-based criteria, with an RMS error of 11 % in the high-cycle fatigue regime and 12.2 % for a fatigue life between 10^4 and 5×10^6 cycles. Additionally, it offers several advantages over these established criteria, including lower sensitivity to mesh size, ease of implementation, and the ability to work with scalars. These benefits make it a highly promising option for practical applications in the industry.

In the future, additional research will be conducted to explore the complex reformulation of the criterion under elastic/plastic conditions. This will be done with the goal of enhancing the accuracy in the low-to-medium-cycle fatigue domain. Furthermore, we anticipate that this criterion can be applied to other metal classes, such as steels or aluminum alloys, by adjusting the strengthening coefficient k_φ to accommodate the material's distinct response to out-of-phase loading.

Appendix A. Fatigue data

A.1. GJS-600 Axial fatigue data

GJS-600

Plain (a)

Axial loading, R=−1

Number of cycles to failure, N_f (cycles)	Stress amplitude, σ_a (MPa)
5000005	160
1838930	160
5000012	160
1075698	180
694293	180
1532626	180
259825	200
517186	200
900404	200
293965	220

137516	220
271244	220
5000004	170
145018	240
2174451	170

GJS-600

Blunt notch (f)

Axial loading, R=−1

Number of cycles to failure, N_f (cycles)	Stress amplitude, σ_a (MPa)
539448	160
260000	160
5000000	100
1631007	140
1058112	140
812422	140
3742955	120
2712425	120

5000000	110
455808	160
5000000	110
5000000	115

GJS-600

Blunt notch (f)

Axial loading, R=0.5

Number of cycles to failure, N_f (cycles)	Stress amplitude, σ_a (MPa)
281968	70
2459220	50
1946112	50
705742	60
5000000	45
178690	75
881573	60
273488	70
3548471	50

GJS-600

Sharp notch (c)

Axial loading, R=−1

Number of cycles to failure, N_f (cycles)	Stress amplitude, σ_a (MPa)
407693	120
368488	120
2327507	100
5000000	100
282475	140
228978	140
5000000	90
4701773	95
5000000	90
417018	120
273662	140
100000	160

GJS-600

Sharp notch 90° (i)

Axial loading, R=0.1

Number of cycles to failure, N_f (cycles)	Stress amplitude, σ_a (MPa)
682557	70
2204029	60
5000000	60
454439	70
2265509	60
1625713	60
2656910	60
2901015	60
1352330	60
5000000	55
5000000	55
5000000	55
2410301	55
2777083	55

891311	70
273768	80
299783	80
385664	80
185040	90
213037	90
187023	90
101563	100
100282	100
87474	100

A.2. GJS-600 Torsional fatigue data

GJS-600

Plain (b)

Torsional loading, R=−1

Number of cycles to failure, N_f (cycles)	Shear stress amplitude, τ_a (MPa)
3000000	160
152000	240

46000	260
534000	200
684669	200
82000	260
2070000	180
940862	180
754196	180
1013395	200
392869	220
3000000	160
210340	240
209996	220

GJS-600

Blunt notch (g)

Torsional loading, R=−1

Number of cycles to failure, N_f (cycles)	Shear stress amplitude, τ_a (MPa)
1960572	200

471522	220
239157	240
2353571	200
791874	220
214739	240
3000000	190
83000	260
3000000	200
90600	260
690738	220
208668	240
77766	260
1619225	210

GJS-600

Blunt notch (g)

Torsional loading, R=0.1

Number of cycles to failure, N_f (cycles)	Shear stress amplitude, τ_a (MPa)

460906	130
2301839	110
700891	130
5000000	100
139002	150
286159	150
1245382	110
1260414	110
591800	130

GJS-600

Sharp notch (d)

Torsional loading, R=−1

Number of cycles to failure, N_f (cycles)	Shear stress amplitude, τ_a (MPa)
2000000	100
2000000	150
70000	220
2000000	180

Number of cycles to failure, N_f (cycles)	Stress amplitude, σ_a (MPa)
5597	270
126125	220
409480	200
2000000	180
17285	250
475383	200
103954	220
763260	190
20038	250
948396	190
775687	190
650000	180

A.3. GJS-600 Multiaxial fatigue data

GJS-600

Plain (b)

Multiaxial loading, λ=1, R=−1, φ=0°

Number of cycles to failure, N_f (cycles)	Stress amplitude, σ_a (MPa)

212099	150
415072	130
1518569	100
1897706	100
2000000	90
182211	130
484191	150
2000000	90
2000000	100
165936	150
61149	170
38332	170
269280	150
338738	130

GJS-600

Plain (b)

Multiaxial loading, λ=1, R=−1, φ=90°

Number of cycles to failure, N_f (cycles)	Stress amplitude, σ_a (MPa)
260432	160
145035	180
3000000	140
781387	150
769140	150
168574	160
36925	180
390240	160
337534	150
2126980	140
43944	180
1373134	140

GJS-600

Blunt notch (h)

Multiaxial loading, λ=1, R=−1, φ=0°

Number of cycles to failure, N_f (cycles)	Stress amplitude, σ_a (MPa)

Number of cycles to failure, N_f (cycles)	Stress amplitude, σ_a (MPa)
127257	140
319681	120
595380	110
2147533	100
423115	100
5000000	80
108931	140
2475139	90
5000000	80
277923	120
5000000	90
1258058	90

GJS-600

Blunt notch (h)

Multiaxial loading, λ=1, R=−1, φ=90°

Number of cycles to failure, N_f (cycles)	Stress amplitude, σ_a (MPa)
5000000	100

257642	150
518204	125
597006	125
5000000	100
5000000	110
751322	125
61284	150
121961	150
239743	137.5
2895375	115
197512	137.5
1020783	115
288376	137.5

GJS-600

Blunt notch (h)

Multiaxial loading, λ=2, R=−1, φ=0°

Number of cycles to failure, N_f (cycles)	Stress amplitude, σ_a (MPa)

207195	80
79986	90
1215835	60
1032688	60
4103365	50
226605	80
102745	90

GJS-600

Blunt notch (h)

Multiaxial loading, λ=2, R=−1, φ=45°

Number of cycles to failure, N_f (cycles)	Stress amplitude, σ_a (MPa)
419909	80
536213	80
5000000	60
1734162	70
235584	90
177844	90

960957	70
58729	100

GJS-600

Blunt notch (h)

Multiaxial loading, λ=2, R=0.1, φ=45°

Number of cycles to failure, N_f (cycles)	Stress amplitude, σ_a (MPa)
1584537	40
366774	50
1510317	40
388806	50
121715	60
2762930	35
120284	60
3089467	35

GJS-600

Sharp notch (e)

Multiaxial loading, λ=1, R=−1, φ=0°

Number of cycles to failure, N_f (cycles)	Stress amplitude, σ_a (MPa)
230649	95
257809	95
121839	95
1672262	80
2000000	80
25443	115
1566089	80
55185	115
5000000	75
234030	95
365066	95
1880865	85
1289763	85
792446	85
249467	95

Number of cycles to failure, N_f (cycles)	Stress amplitude, σ_a (MPa)
2000000	80
51000	115
2000000	80
43913	115
448817	90
168000	90

GJS-600

Sharp notch (e)

Multiaxial loading, λ=1, R=−1, φ=90°

Number of cycles to failure, N_f (cycles)	Stress amplitude, σ_a (MPa)
2552155	100
637181	120
83523	140
100028	140
5000000	90
52141	140
1988821	100

2423709	100
367334	120
784273	110
326603	120
733855	110

A.4. HSi Axial fatigue data

HSi Plain (a) Axial loading, R=−1	
Number of cycles to failure, N_f (cycles)	**Stress amplitude, σ_a (MPa)**
5000010	170
5000011	190
310008	230
453442	230
141703	250
139712	250
1135517	210

830609	210
1708075	210
5000005	170
359115	250
5000005	190
280816	270
2768109	190
5000011	180
151030	270
1441356	200
4391109	180
5000002	180
36850	290
5000011	180
13699	290
5000015	180
64710	290

5000008	190
48391	290
5000004	200
361467	210
176156	270
50693	270
690228	200

HSi

Plain (a)

Axial loading, R=0.1

Number of cycles to failure, N_f (cycles)	Stress amplitude, σ_a (MPa)
909335	120
1429112	120
1104738	120
10000013	110
49331	160
305680	140

300567	140
300186	140
10000004	110
76808	160
10000004	110
99804	160
56135	160
106447	160
89653	160

HSi

Blunt notch (f)

Axial loading, R=−1

Number of cycles to failure, N_f (cycles)	Stress amplitude, σ_a (MPa)
570242	110
1348704	100
5000000	90
2725278	95

1775266	95
4215742	90
1116515	100
801265	120
208130	130
4352468	90
961895	120
273719	130
497616	110

HSi

Sharp notch (c)

Axial loading, R=−1

Number of cycles to failure, N_f (cycles)	Stress amplitude, σ_a (MPa)
314452	130
169101	130
1130698	110
4759547	90

3499493	90
843296	110
5000005	80
5000017	80
255091	130
5000019	85
5000013	90
1593028	100
2310181	100

HSi

Sharp notch (c)

Axial loading, R=0.5

Number of cycles to failure, N_f (cycles)	Stress amplitude, σ_a (MPa)
5000000	40
713707	50
5000000	45
1424451	55

1051000	50
1807855	45
299162	65
152594	75
3859594	45
734224	55
217979	55
529635	65
182520	75

A.5. HSi Torsional fatigue data

HSi

Plain (b)

Torsional loading, R=−1

Number of cycles to failure, N_f (cycles)	Shear stress amplitude, τ_a (MPa)
3780956	160
2960414	150
1525557	180

2968176	160
479056	180
1511928	180
1320674	200
1303674	160
709364	200
147346	220
300553	220
274515	240

HSi

Blunt notch (g)

Torsional loading, R=−1

Number of cycles to failure, N_f (cycles)	Shear stress amplitude, τ_a (MPa)
550637	200
490687	200
582136	200
124250	220

127412	220
1364011	180
1504460	180
1283849	180
2122528	170
3455409	160

HSi

Blunt notch (g)

Torsional loading, R=0.1

Number of cycles to failure, N_f (cycles)	Shear stress amplitude, τ_a (MPa)
5000000	100
222000	140
1014513	120
440521	140
1572345	120
2333850	120
581922	140

157881	160
68946	160

HSi

Sharp notch (d)

Torsional loading, R=−1

Number of cycles to failure, N_f (cycles)	Shear stress amplitude, τ_a (MPa)
1138020	190
1196418	190
517271	210
361986	210
1138249	190
1789935	180
2176289	180
202240	230
191694	230
527483	210
4219051	170

1900286	180

A.6. HSi Multiaxial fatigue data

HSi

Plain (b)

Multiaxial loading, λ=1, R=−1, φ=0°

Number of cycles to failure, N_f (cycles)	Stress amplitude, σ_a (MPa)
2257723	100
5000000	100
843076	120
1756329	120
325651	140
2161359	120
598682	140
326765	140
92937	160
182454	160
97870	160

4559484	100

HSi

Plain (b)

Multiaxial loading, λ=1, R=−1, φ=90°

Number of cycles to failure, N_f (cycles)	Stress amplitude, σ_a (MPa)
1182000	140
422188	160
99000	180
481310	140
482506	140
236509	160
2277200	120
206740	160
5000000	120
89753	180
3202101	120
98137	180

HSi

Blunt notch (h)

Multiaxial loading, λ=1, R=−1, φ=0°

Number of cycles to failure, N_f (cycles)	Stress amplitude, σ_a (MPa)
305405	100
291264	100
337136	100
856643	80
685152	80
668174	80
89904	120
100068	120
2500000	70
1836000	70
2281000	70
5000000	60
264694	100

HSi

Blunt notch (h)

Multiaxial loading, λ=1, R=−1, φ=90°

Number of cycles to failure, N_f (cycles)	Stress amplitude, σ_a (MPa)
484239	100
5000000	80
2421352	90
2546960	90
1786072	90
5000000	80
817547	100
509923	110
412791	110
285501	120
842368	100

HSi

Sharp notch (e)

Multiaxial loading, λ=1, R=−1, φ=0°

Number of cycles to failure, N_f (cycles)	Stress amplitude, σ_a (MPa)
710070	90
768201	90
730173	90
5000000	70
1828873	70
1935893	70
175151	110
151780	110
154258	110
52044	130
52248	130

HSi

Sharp notch (e)

Multiaxial loading, λ=1, R=−1, φ=90°

Number of cycles to failure, N_f (cycles)	Stress amplitude, σ_a (MPa)
1898888	90
1598072	90
395081	110
356010	110
393402	110
5000000	80
17789	130
17267	130
45660	120
29674	120

A.4. GJS-400 Axial fatigue data

GJS-400

Plain (j)

Axial loading, R=−1

Number of cycles to failure, N_f (cycles)	Stress amplitude, σ_a (MPa)
100520	160

3000000	140
805352	160
21585	200
14980	200
262928	160
1671517	150
3000000	150
277501	180

GJS-400

Plain (j)

Axial loading, R=0

Number of cycles to failure, N_f (cycles)	Stress amplitude, σ_a (MPa)
27299	120
562940	100
439778	90
2967983	90
1493548	80

3000000	70
3000000	80
13822	120

GJS-400

Sharp notch (k)

Axial loading, R=−1

Number of cycles to failure, N_f (cycles)	Stress amplitude, σ_a (MPa)
159000	130
408667	108.5
2000000	80
86632	160
1091520	108.5
193903	130
40194	160

GJS-400

Sharp notch (k)

Axial loading, R=0.05

Number of cycles to failure, N_f (cycles)	Stress amplitude, σ_a (MPa)
136081	80
1389281	60
3000000	50
46121	100
3000000	60
709456	70

A.5. GJS-400 Torsional fatigue data

GJS-400

Plain (j)

Torsional loading, R=−1

Number of cycles to failure, N_f (cycles)	Shear stress amplitude, τ_a (MPa)
1997292	140
174802	180
1465636	140
12900	220

174965	180
22681	220
29571	200
77203	200
347217	160
359370	160
2380226	140
280117	160

GJS-400

Plain (j)

Torsional loading, R=0

Number of cycles to failure, N_f (cycles)	Shear stress amplitude, τ_a (MPa)
1517	180
24981	160
69549	140
995771	80
2235000	80

72

845935	100
572822	100
119857	120

GJS-400

Sharp notch (k)

Torsional loading, R=−1

Number of cycles to failure, N_f (cycles)	Shear stress amplitude, τ_a (MPa)
350000	180
5055500	140
3698000	140
10000	220
38500	200
285000	180
980000	160
338500	180
45750	200

GJS-400

Sharp notch (k)

Torsional loading, R=0

Number of cycles to failure, N_f (cycles)	Shear stress amplitude, τ_a (MPa)
61890	140
5000000	80
5000000	100
73000	140
286830	130
1663000	110
597350	120
1720000	110
21000	150

A.6. GJS-400 Multiaxial fatigue data

GJS-400

Plain (j)

Multiaxial loading, λ=1, R=−1, φ=0°

Number of cycles to failure, N_f (cycles)	Stress amplitude, σ_a (MPa)

74

127708	120
716772	100
53359	140
2300000	80
11272	160
16264	160
781172	100
141804	120
643539	90
1694317	90
2600000	80

GJS-400

Plain (j)

Multiaxial loading, λ=1, R=−1, φ=90°

Number of cycles to failure, N_f (cycles)	Stress amplitude, σ_a (MPa)
29000	160
305000	120

2500000	100
6500	180
350000	110

GJS-400

Sharp notch (k)

Multiaxial loading, λ=1, R=−1, φ=0°

Number of cycles to failure, N_f (cycles)	Stress amplitude, σ_a (MPa)
229000	100
1361500	80
68500	90
520000	90
297500	100
5000000	70
1998000	80
602000	90
46800	120
28500	130

103000	110
16400	140

GJS-400

Sharp notch (k)

Multiaxial loading, λ=1, R=−1, φ=90°

Number of cycles to failure, N_f (cycles)	Stress amplitude, σ_a (MPa)
56700	100
10440	120
9300	100
620000	90
1104000	90
17500	110
30000	100
16500	110
10100	120
444900	90
607000	90

472480	95
1200000	85

GJS-400

Sharp notch (k)

Multiaxial loading, λ=1, R=0, φ=0°

Number of cycles to failure, N_f (cycles)	Stress amplitude, σ_a (MPa)
43525	80
20535	90
1410000	60
180000	70
173000	70
9000	100
1040000	60

GJS-400

Sharp notch (k)

Multiaxial loading, λ=1, R=0, φ=90°

Number of cycles to failure, N_f (cycles)	Stress amplitude, σ_a (MPa)
99000	70
15500	90
1315000	60
35000	80
69000	70
510000	60

GJS-400

Sharp notch (k)

Multiaxial loading, λ=0.6, R=−1, φ=0°

Number of cycles to failure, N_f (cycles)	Stress amplitude, σ_a (MPa)
50500	140
170000	120
5000000	80
2700000	100
494000	110

GJS-400

Sharp notch (k)

Multiaxial loading, λ=0.6, R=−1, φ=90°

Number of cycles to failure, N_f (cycles)	Stress amplitude, σ_a (MPa)
22630	140
598500	100
47200	120
165000	110

References

[1] Bleicher C, Kaufmann H, Melz T. Assessment of service loads and material influence on the lifetime of thick-walled nodular cast iron components. Int J Fatigue 2021;147:106171. https://doi.org/10.1016/J.IJFATIGUE.2021.106171.

[2] Benedetti M, Santus C, Raghavendra S, Lusuardi D, Zanini F, Carmignato S. Multiaxial plain and notch fatigue strength of thick-walled ductile cast iron EN-GJS-600-3: Combining multiaxial fatigue criteria, theory of critical distances, and defect sensitivity. Int J Fatigue 2022;156. https://doi.org/10.1016/j.ijfatigue.2021.106703.

[3] Onsøien MI, Skaland T, Jørgensen K. Mechanisms of graphite formation in ductile cast iron containing rare earth metals. Materials Science and Technology 1999;15. https://doi.org/10.1179/026708399101505815.

[4] Riposan I, Chisamera M, Uta V, Stan S, Naro R, Williams D. The Importance of Rare Earth Contribution from Nodulizing Alloys and their Subsequent Effect on the Inoculation of Ductile Iron. International Journal of Metalcasting 2014;8. https://doi.org/10.1007/BF03355583.

[5] Papadopoulos I. A comparative study of multiaxial high-cycle fatigue criteria for metals. Int J Fatigue 1997;19. https://doi.org/10.1016/S0142-1123(96)00064-3.

[6]   Crossland B. Effect of large hydrostatic pressures on the torsional fatigue strength of an alloy steel. International conference on the fatigue of metals, London: Institution of Mechanical Engineers; 1956, p. 138–49.

[7]   Sines G. Metal Fatigue. New York: McGraw-Hill; 1959.

[8]   Carpinteri A, Spagnoli A, Vantadori S. Multiaxial fatigue assessment using a simplified critical plane-based criterion. Int J Fatigue 2011;33:969–76. https://doi.org/10.1016/J.IJFATIGUE.2011.01.004.

[9]   Findley WN. A Theory for the Effect of Mean Stress on Fatigue of Metals Under Combined Torsion and Axial Load or Bending. Journal of Engineering for Industry 1959;81. https://doi.org/10.1115/1.4008327.

[10]   Matake T. An Explanation on Fatigue Limit under Combined Stress. Bulletin of JSME 1977;20. https://doi.org/10.1299/jsme1958.20.257.

[11]   Stanfield G. Discusson on "The strength of metals under combined alternating stresses." In: Gough H, Pollard H, editors. Proc. Inst. Mech. Eng. 131, 1935, p. 93.

[12]   Brown MW, Miller KJ. A Theory for Fatigue Failure under Multiaxial Stress-Strain Conditions. Proceedings of the Institution of Mechanical Engineers 1973;187. https://doi.org/10.1243/PIME_PROC_1973_187_161_02.

[13]   Commission of the European Communities. Joint Research Centre. Ispra Establishment., Metals Society., Associazione italiana di metallurgia., American Society for Metals. Mechanical behaviour and nuclear applications of stainless steel at elevated temperatures : proceedings of the international conference. Metals Society; 1982.

[14]   J.L. R. Contribution à l'étude de la fatigue multi axiale sous sollicitations periodiques ou aléatoire. 1992.

[15]   McDiarmid DL. A general criterion for high cycle multiaxial fatigue failure. Fatigue Fract Eng Mater Struct 1991;14. https://doi.org/10.1111/j.1460-2695.1991.tb00673.x.

[16]   McDiarmid DL. A shear stress based critical-plane criterion of multiaxial fatigue failure for design and life prediction. Fatigue Fract Eng Mater Struct 1994;17. https://doi.org/10.1111/j.1460-2695.1994.tb00789.x.

[17]   Fatemi A, Socie DF. A critical plane approach to multiaxial fatigue damage including out-of-phase loading. Fatigue Fract Eng Mater Struct 1988;11. https://doi.org/10.1111/j.1460-2695.1988.tb01169.x.

[18]   Ince A, Glinka G. A generalized fatigue damage parameter for multiaxial fatigue life prediction under proportional and non-proportional loadings. Int J Fatigue 2014;62:34–41. https://doi.org/10.1016/J.IJFATIGUE.2013.10.007.

[19]   Ince A, Glinka G. Innovative computational modeling of multiaxial fatigue analysis for notched components. Int J Fatigue 2016;82:134–45. https://doi.org/10.1016/J.IJFATIGUE.2015.03.019.

[20]   Yu Q, Zhang J, Jiang Y, Li Q. Multiaxial fatigue of extruded AZ61A magnesium alloy. Int J Fatigue 2011;33:437–47. https://doi.org/10.1016/J.IJFATIGUE.2010.09.020.

[21]   Liu J, Zhang Z, Li B, Lang S. Multiaxial Fatigue Life Prediction of GH4169 Alloy Based on the Critical Plane Method. Metals (Basel) 2019;9. https://doi.org/10.3390/met9020255.

[22]   Zhong B, Wang Y, Wei D, Wang J. A new life prediction model for multiaxial fatigue under proportional and non-proportional loading paths based on the pi-plane projection. Int J Fatigue 2017;102:241–51. https://doi.org/10.1016/J.IJFATIGUE.2017.04.013.

[23]   Bannantine J, Socie D. A variable amplitude multiaxial fatigue life prediction method. Fatigue under biaxial and multiaxial loading, 1989, p. 35–51.

[24]   Smith KN, Watson P, Topper TH. A Stress-Strain Function for the Fatigue of Metals. J Mater 1970;5:767–78.

[25]   Liu K. A Method Based on Virtual Strain-Energy Parameters for Multiaxial Fatigue Life Prediction. Advances in Multiaxial Fatigue, 100 Barr Harbor Drive, PO Box C700, West Conshohocken, PA 19428-2959: ASTM International; n.d. https://doi.org/10.1520/STP24796S.

[26]   Sun C, Song Q. A Method for Predicting the Effects of Specimen Geometry and Loading Condition on Fatigue Strength. Metals (Basel) 2018;8. https://doi.org/10.3390/met8100811.

[27]   Jiang Y, Hertel O, Vormwald M. An experimental evaluation of three critical plane multiaxial fatigue criteria. Int J Fatigue 2007;29:1490–502. https://doi.org/10.1016/J.IJFATIGUE.2006.10.028.

[28]   Chu C-C. Fatigue Damage Calculation Using the Critical Plane Approach. J Eng Mater Technol 1995;117. https://doi.org/10.1115/1.2804370.

[29]   Chu C-C, Conle F, Bonnen J. Multiaxial Stress-Strain Modeling and Fatigue Life Prediction of SAE Axle Shafts. Advances in Multiaxial Fatigue, 100 Barr Harbor Drive, PO Box C700, West Conshohocken, PA 19428-2959: ASTM International; n.d. https://doi.org/10.1520/STP24794S.

[30]   Berto F, Lazzarin P. Recent developments in brittle and quasi-brittle failure assessment of engineering materials by means of local approaches. Materials Science and Engineering: R: Reports 2014;75. https://doi.org/10.1016/j.mser.2013.11.001.

[31]   Neuber, Heinz. Kerbspannungslehre. Springer, Berlin Heidelberg; 1985.

[32] Lazzarin P, Zambardi R. A finite-volume-energy based approach to predict the static and fatigue behavior of components with sharp V-shaped notches. Int J Fract 2001;112. https://doi.org/10.1023/A:1013595930617.

[33] Berto F, Lazzarin P, Yates JR. Multiaxial fatigue of V-notched steel specimens: A non-conventional application of the local energy method. Fatigue Fract Eng Mater Struct 2011;34:921–43. https://doi.org/10.1111/j.1460-2695.2011.01585.x.

[34] Tanaka K. Crack initiation and propagation in torsional fatigue of circumferentially notched steel bars. Int J Fatigue 2014;58:114–25. https://doi.org/10.1016/j.ijfatigue.2013.01.002.

[35] Susmel L, Berto F, Hu Z. The Strain energy density to estimate lifetime of notched components subjected to variable amplitude fatigue loading. Frattura Ed Integrità Strutturale 2018;13:383–93. https://doi.org/10.3221/IGF-ESIS.47.28.

[36] Atzori B, Berto F, Lazzarin P, Quaresimin M. Multi-axial fatigue behaviour of a severely notched carbon steel. Int J Fatigue 2006;28. https://doi.org/10.1016/j.ijfatigue.2005.05.010.

[37] Benedetti M, Berto F, Le Bone L, Santus C. A novel Strain-Energy-Density based fatigue criterion accounting for mean stress and plasticity effects on the medium-to-high-cycle uniaxial fatigue strength of plain and notched components. Int J Fatigue 2020;133. https://doi.org/10.1016/j.ijfatigue.2019.105397.

[38] Marangon C, Lazzarin P, Berto F, Campagnolo A. Some analytical remarks on the influence of phase angle on stress fields ahead of sharp V-notches under tension and torsion loads. Theoretical and Applied Fracture Mechanics 2014;74. https://doi.org/10.1016/j.tafmec.2014.06.015.

[39] Sonsino CM, Grubisic V. Multiaxial fatigue behaviour of Sintered Steels under combined in and out of phase bending and torsion. Materwiss Werksttech 1987;18. https://doi.org/10.1002/mawe.19870180506.

[40] Kueppers M, Sonsino CM. Assessment of the fatigue behaviour of welded aluminium joints under multiaxial spectrum loading by a critical plane approach. Int J Fatigue 2006;28:540–6. https://doi.org/10.1016/J.IJFATIGUE.2005.07.046.

[41] Berto F, Lazzarin P, Tovo R. Multiaxial fatigue strength of severely notched cast iron specimens. Int J Fatigue 2014;67. https://doi.org/10.1016/j.ijfatigue.2014.01.013.

[42] Tovo R, Lazzarin P, Berto F, Cova M, Maggiolini E. Experimental investigation of the multiaxial fatigue strength of ductile cast iron. Theoretical and Applied Fracture Mechanics 2014;73:60–7. https://doi.org/10.1016/J.TAFMEC.2014.07.003.

[43] Itoh T, Sakane M, Ohsuga K. Multiaxial low cycle fatigue life under non-proportional loading. International Journal of Pressure Vessels and Piping 2013;110:50–6. https://doi.org/10.1016/J.IJPVP.2013.04.021.

[44] Benedetti M, Santus C, Fontanari V, Lusuardi D, Zanini F, Carmignato S. Plain and notch fatigue strength of thick-walled ductile cast iron EN-GJS-600-3: A double-notch critical distance approach to defect sensitivity. Int J Fatigue 2021;152. https://doi.org/10.1016/j.ijfatigue.2021.106414.

[45] Pedranz M, Fontanari V, Raghavendra S, Santus C, Zanini F, Carmignato S, et al. A new energy based highly stressed volume concept to investigate the notch-pores interaction in thick-walled ductile cast iron subjected to uniaxial fatigue. Int J Fatigue 2023;169:107491. https://doi.org/10.1016/J.IJFATIGUE.2022.107491.

[46] Borsato T, Ferro P, Berto F. Novel method for the fatigue strength assessment of heavy sections made by ductile cast iron in presence of solidification defects. Fatigue Fract Eng Mater Struct 2018;41. https://doi.org/10.1111/ffe.12815.

[47] Santus C, Taylor D, Benedetti M. Determination of the fatigue critical distance according to the Line and the Point Methods with rounded V-notched specimen. Int J Fatigue 2018;106. https://doi.org/10.1016/j.ijfatigue.2017.10.002.

[48] Santus C, Berto F, Pedranz M, Benedetti M. Mode III critical distance determination with optimized V-notched specimen under torsional fatigue and size effects on the inverse search probability distribution. Int J Fatigue 2021;151. https://doi.org/10.1016/j.ijfatigue.2021.106351.

[49] Haibach E. Betriebsfestigkeit. Berlin/Heidelberg: Springer-Verlag; 2006. https://doi.org/10.1007/3-540-29364-7.

[50] Störzel K, Baumgartner J. Statistical evaluation of fatigue tests using maximum likelihood. Materials Testing 2021;63:714–20. https://doi.org/10.1515/mt-2020-0116.

[51] Borsato T, Berto F, Ferro P, Carollo C. Influence of solidification defects on the fatigue behaviour of heavy-section silicon solution-strengthened ferritic ductile cast irons. Fatigue Fract Eng Mater Struct 2018;41. https://doi.org/10.1111/ffe.12810.

[52] Stefanescu DM. Computer simulation of shrinkage related defects in metal castings – a review. International Journal of Cast Metals Research 2005;18:129–43. https://doi.org/10.1179/136404605225023018.

[53] Sonsino CM, Kuepper M. Fatigue behaviour of welded aluminium under multiaxial loading. Sixth International Conference on Biaxial/Multiaxial Fatigue and Fracture, ESIS; 2001, p. 57–64.

[54] Banvillet A. A volumetric energy based high cycle multiaxial fatigue citerion. Int J Fatigue 2003;25. https://doi.org/10.1016/S0142-1123(03)00048-3.

[55] Sonsino CM. Influence of Material Ductility on Fatigue Life under Multiaxial Proportional and Non-Proportional Normal and Shear Stresses. MATEC Web of Conferences 2019;300:17001. https://doi.org/10.1051/matecconf/201930017001.

[56] Grubisic V, Neugebauer J. Fatigue Behaviour of Nodular Cast Iron under Multiaxial Loadings. Giessereiforschung 1979;31:123–8.

[57] Müller A. Fatigue Behaviour of Nodular and Tempered Cast Iron under Multiaxial Random Loadings. Darmstadt, Germany, Report No. FB-203: 1994.

[58] Benedetti M, Santus C, Berto F. Inverse determination of the fatigue Strain Energy Density control radius for conventionally and additively manufactured rounded V-notches. Int J Fatigue 2019;126:306–18. https://doi.org/10.1016/j.ijfatigue.2019.04.040.

[59] Benedetti M, Dallago M, Santus C. Statistical significance of notch fatigue prognoses based on the strain-energy–density method: Application to conventionally and additively manufactured materials. Theoretical and Applied Fracture Mechanics 2020;109. https://doi.org/10.1016/j.tafmec.2020.102720.

[60] Benedetti M, Pedranz M, Berto F, Santus C. Inverse determination and probability distribution of the mode III Strain Energy Density control radius with an optimized V-notched specimen under torsional fatigue loading. Int J Fatigue 2022. https://doi.org/10.1016/j.ijfatigue.2022.106787.

[61] Berto F, Lazzarin P. A review of the volume-based strain energy density approach applied to V-notches and welded structures. Theoretical and Applied Fracture Mechanics 2009;52. https://doi.org/10.1016/j.tafmec.2009.10.001.

[62] Berto F. A Brief Review of Some Local Approaches for the Failure Assessment of Brittle and Quasi-Brittle Materials. Advances in Materials Science and Engineering 2014;2014. https://doi.org/10.1155/2014/930679.

[63] Murakami Y. Metal fatigue. Effects of small defects and nonmetallic inclusions. 2nd Edition. Oxford: Elsevier; 2002.

[64] Ferro P, Lazzarin P, Berto F. Fatigue properties of ductile cast iron containing chunky graphite. Materials Science and Engineering: A 2012;554. https://doi.org/10.1016/j.msea.2012.06.024.

[65] Vaara J, Väntänen M, Laine J, Kemppainen J, Frondelius T. Prediction of the fatigue limit defining mechanism of nodular cast iron based on statistical microstructural features. Eng Fract Mech 2023;277. https://doi.org/10.1016/j.engfracmech.2022.109004.

[66] Endo M. Effects of graphite shape, size and distribution on the fatigue strength of spheroidal graphite cast irons. Journal of the Society of Materials Science, Japan 1989;38. https://doi.org/10.2472/jsms.38.1139.

[67] Endo M, Yanase K. Effects of small defects, matrix structures and loading conditions on the fatigue strength of ductile cast irons. Theoretical and Applied Fracture Mechanics 2014;69. https://doi.org/10.1016/j.tafmec.2013.12.005.

[68] Endo M, Matsuo T. A practical method for fatigue limit prediction in ductile cast irons. Fatigue Fract Eng Mater Struct 2019;42. https://doi.org/10.1111/ffe.13086.

[69]   Endo M, Wanf X-B. Special Issue on Fracture Mechanics. Effects of Graphite and Artificial Small Defect on theFatigue Strength of Current Ductile Cast Irons. Journal of the Society of Materials Science, Japan 1994;43. https://doi.org/10.2472/jsms.43.1245.

[70]   Dowling NE, Calhoun CA, Arcari A. Mean stress effects in stress-life fatigue and the Walker equation. Fatigue Fract Eng Mater Struct 2009;32:163–79. https://doi.org/10.1111/j.1460-2695.2008.01322.x.

[71]   Burger R, Lee Y-L. Assessment of the Mean-Stress Sensitivity Factor Method in Stress-Life Fatigue Predictions. J Test Eval 2013;41:20120035. https://doi.org/10.1520/JTE20120035.

[72]   Susmel L, Lazzarin P. A bi-parametric Wöhler curve for high cycle multiaxial fatigue assessment. Fatigue Fract Eng Mater Struct 2002;25. https://doi.org/10.1046/j.1460-2695.2002.00462.x.

- Multiaxial synchronous fatigue tests carried out on three different ductile cast iron grades.
- Multiaxial fatigue criterion based on the volumetric strain energy density.
- The mean stress effect is accounted by a combination of the stress amplitude and the maximum stress.
- Formulation of the phase effect for ductile cast irons by means of a phase correction factor.
- Accurate predictions with an RMS error at 5 million cycles of 11.0 %.

Matteo Pedranz: Conceptualization, Methodology, Investigation, Writing - Original Draft, Writing - Review & Editing. **Matteo Benedetti:** Methodology, Writing - Original Draft, Writing - Review & Editing, Supervision, Investigation. **Vigilio Fontanari**: Methodology, Writing - Review & Editing, Supervision. **Danilo Lusuardi:** Resources, Supervision. **Ciro Santus:** Methodology, Writing - Review & Editing. **Filippo Berto:** Methodology, Writing - Review & Editing, Investigation.

Declaration of interests

☒The authors declare that they have no known competing financial interests or personal relationships that could have appeared to influence the work reported in this paper.

☐The authors declare the following financial interests/personal relationships which may be considered as potential competing interests: